

TECHNOLOGY DEVELOPMENT FOR EXOPLANET MISSIONS

Technology Milestone Whitepaper

JPL Document D-68672

ADVANCING TECHNOLOGY FOR STARLIGHT SUPPRESSION VIA AN EXTERNAL OCCULTER

PROF. N. JEREMY KASDIN
PRINCIPAL INVESTIGATOR
PRINCETON UNIVERSITY
MECHANICAL AND AEROSPACE ENGINEERING

January 24, 2011

CoInvestigators:

David N. Spergel (Science PI), Princeton University, Robert Vanderbei, Princeton University, Stuart Shaklan (Institutional PI), Jet Propulsion Laboratory, Phil Dumont, Jet Propulsion Laboratory, Domenick Tenerelli (Institutional PI), Lockheed-Martin, Julie Mikula (Institutional PI), NASA Ames Research Center, Bruce Macintosh (Institutional PI), Lawrence Livermore National Laboratory, Robert Rudd, Lawrence Livermore National Laboratory, Roger Linfield (Institutional PI), Ball Aerospace, Sarah Lipscey, Ball Aerospace

Other Key Personnel:

Doug Lisman, Mark Thompson, Eric Cady, Jet Propulsion Laboratory, Dave Putnam, Sean McCully, John Miles, Lockheed-Martin, Dmitry Savransky, Princeton University

Approvals

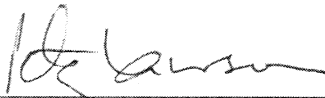
Released by:



03/01/2011

N. Jeremy Kasdin
Principal Investigator, Princeton University

Approved by:



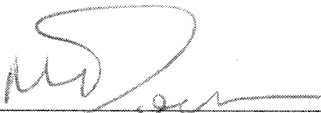
3/9/2011

Peter R. Lawson
Exoplanet Exploration Program Chief Technologist, JPL



4/6/2011

Marie Levine
Exoplanet Exploration Technology Manager, JPL



4/12/2011

Michael Devirian
Exoplanet Exploration Program Manager, JPL



4/14/2011

Douglas Hudgins
Exoplanet Exploration Program Scientist, NASA HQ



4/12/2011

Lia LaPiana
Exoplanet Exploration Program Executive, NASA HQ

CONTENTS

1. Objective	4
2. Background	5
2.1. Occulter Design	8
2.2. Error Budgeting and Requirements Development	12
2.3. Mechanical Design and Manufacturing	16
2.4. Optical Edge	21
2.5. Materials Selection and Testing	22
2.6. Integrated Modeling	23
3. Milestone Description	26
3.1. Milestone Definition	26
3.2. Summary of Requirements	26
3.3. Precision Edge Metrology	27
3.4. Measurement Analysis Approach	29
3.5. Predicting Contrast	33
4. Success Criteria	38
5. Certification	39
Appendix A. On the assumptions made calculating occulter electric fields with a Bessel function expansion	39
Appendix B. Future Technology Development	41
References	43

1. OBJECTIVE

In support of NASA's Exoplanet Exploration Program and the ROSES Technology Development for Exoplanet Missions (TDEM), this whitepaper explains the TDEM Milestone for external occulter manufacturing and test, specifies the methodology for computing the milestone metric, and establishes the success criteria against which the milestone will be evaluated. Our goal is to advance the readiness of the riskiest key technology associated with occulter-based planet finding and characterization—manufacturing a large starshade to the needed accuracy. *Our objective is to, for the first time, build a full-scale occulter petal, using flight-like processes and materials, and to near-flight tolerances as they are presently understood.* We will perform metrology to confirm that the critical shape requirements have been met and a modeled prediction of the resulting starlight suppression reaches our goal. The work under this TDEM is limited to this *manufacturing demonstration only*.

There are, of course, many other critical engineering technologies that need to be studied and verified to eventually have confidence in the success of an occulter mission. These include starshade stowage and deployment, thermal verification of full-size starshades, optical scatter off the edge, sensing schemes for positioning, demonstrated algorithms for formation flying, and design reference mission analyses with algorithms for planet identification. We postpone all of these to future studies, though the design we are using is a flight design whose kinematics have been demonstrated in a preliminary deployment test.

Building and measuring a petal, as we do in this TDEM study, does address one of the most critical aspect of occulter manufacture—the petals, with their sharp and precisely defined edges, are responsible for diffracting starlight away from the receiving telescope while the telescope looks slightly off to the side of the occulter to see a planet (see Section 2.1). While the required positional precision of a petal relative to the central supporting truss is not trivial (a few hundred microns), this is not viewed as a very challenging requirement. Many perimeter trusses with comparable requirements are already in orbit.

To set the requirements on how well the petal shape must be manufactured we use a variety of modeling tools. Central is our diffractive modeling code (described in Section 2.2.1) that we use to develop an error budget based on various convenient expansions of the petal shape (see Section 2.2.2). By examining the optical performance in the image plane of the telescope, we place bounds on the allowable deviations of each term. Our initial expansions (a combination of polynomials and Fourier components) were chosen for ease of analysis, not necessarily because they were consistent with the kinds of errors one would expect to see during manufacture (see Section 2.3 for details of the mechanical design and manufacture). Nevertheless, they provide important insights into the accuracy and precision with which an occulter must be manufactured and measured and to the most critical categories of errors. This helps us define the design, compare to the integrated models, develop manufacturing processes, and determine the needed accuracy of the metrology system. *An important goal of this TDEM beyond the manufacture of the petal is the formulation of the error budget in a manner consistent with the metrology and fabrication approaches.*

The ultimate objective is to know that the starshade petals have been manufactured with the needed accuracy to achieve the desired contrast in the image plane of the telescope.¹ We thus formulate a milestone that uses the measured shape of the as-built petal and the known accuracy of the metrology system to predict the expected contrast were a starshade to be built with petals of that shape. We simulate a full starshade populated by identical petals as the manufactured one. We then use our optical modeling tools to propagate an incident field to the image plane of the

¹By contrast here we mean the ratio of the residual intensity in the pixels containing the peak of the planet point spread function to the intensity in the pixels containing the peak of the stellar point spread function that would be measured with the same exposure time if the occulter were not present.

telescope and predict the resulting contrast. We repeat a sufficient number of times to give us statistical confidence in our predicted contrast. We choose a relaxed requirement from flight of 10^{-9} total contrast (3×10^{-10} allocated) as our success criteria as this is the first time any petal will have been built to flight tolerances so a relaxed requirement is appropriate. Our milestone can thus be stated:

TDEM Occulter Milestone:

- On a single full-scale petal made of flight-like materials, measure the edge position relative to a fiducial origin at a sufficient number of locations along the edge. Using our optical modeling tools, verify that the predicted mean contrast in the image plane from a uniform field propagated past an occulter with petals of the measured shape in an annulus of width equal to the full-width half-max of the telescope point spread function at the smallest inner working angle is 3×10^{-10} or better, the allocated contrast to static errors. Repeat the measurements and analysis a sufficient number of times to give 95% confidence that the predicted contrast is correct.

The completion of this milestone will be documented in a report by the Principal Investigator and reviewed by NASA HQ.

We will accomplish this milestone by using our optimization tools to design an occulter for a small scale mission (Section 2.1). We will perform an error analysis on the resulting occulter shape design (Section 2.2.1) to produce a nominal error budget (Section 2.2.2). Our mechanical design approach for a foldable occulter is described in Section 2.3 and the design of the “optical edge” of the occulter, which defines the final shape and scatters sunlight away from the telescope, is described in Section 2.4. We have a materials program planned (Section 2.5) to pick the best flight material with the required low coefficient of thermal expansion (CTE) and other mechanical properties. We use our integrated thermal and mechanical modeling tools (Section 2.6) to confirm that the resulting design meets the error budgets in its operating environment (both thermal and dynamic) and as feedback for the mechanical design itself.

After summarizing the milestone (Section 3.1) we delineate the requirements on the static occulter shape derived from the error budget in Section 3.2. We then describe the metrology process that we will use to measure the edge shape in Section 3.3 and our approach to computing contrast in Section 3.5. Our final success criteria for the milestone are listed in Section 4 and the provided data package is described in Section 5.

2. BACKGROUND

The central science goal of the exoplanet research community is the detection and characterization of Earth-like planets. This is a formidable task; planets are much fainter than their host stars and are often at small angular separations. In particular, Earth-like planets—that is, rocky planets in habitable zones—are estimated to be 10^{10} times dimmer than the stars they orbit [1], and to be located at angular separations of a hundred milliarcseconds or less from the closest stars.

There are many approaches to creating the contrast in the image plane of a telescope needed for exoplanet exploration, most of which use either an internal coronagraph or an external occulter.[2] All approaches have the potential to yield similar exoplanet science (measured in number of planets discovered and characterized) at a flagship scale, yet each has different technical challenges. In this whitepaper we focus on an external occulter mission concept, a spacecraft with a shaped edge flown in formation with a telescope (see Figure 1), as a plausible mission architecture that could be flown in the next decade if the technology is sufficiently advanced. The size, shape, and separation of the occulter are chosen so that it suppresses the light from the star by more than ten orders

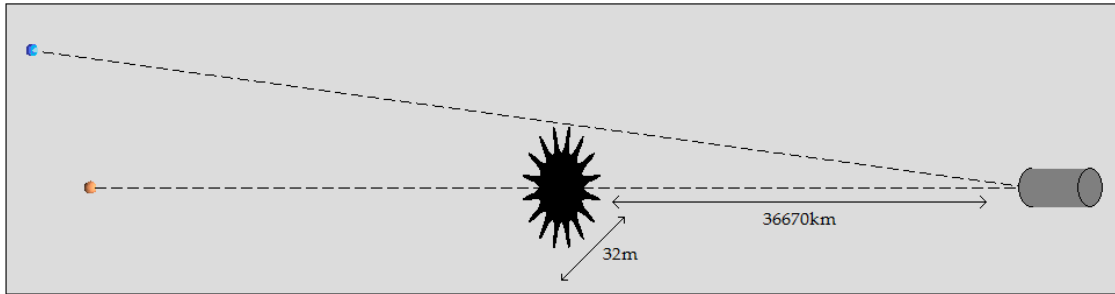


FIGURE 1. A schematic diagram of a representative occulter flying in formation with a telescope to provide starlight suppression and enable imaging of a companion exoplanet at a small geometric inner working angle. The orange source is a star, and the blue source a planetary companion.

of magnitude over a particular wavelength band, while leaving the planet light unaffected. Most designs have the occulter tens of meters in diameter, and separated from the telescope by tens of thousands of kilometers, which gives the occulter an angular size on the order of a hundred milliarcseconds.

Lyman Spitzer was the first to suggest using a smoothly apodized screen to block starlight (the apodization is critical as it limits light diffracting into the shadow area).[3] Recently, a number of approaches have been proposed for finding apodizations that produce sufficient starlight suppression.[4, 5, 6] Unfortunately, it is virtually impossible to manufacture any smoothly apodized occulter with sufficient precision. We therefore approximate the apodized screen with a binary occulter, which allows either all or none of the light through at any point. The resulting shape has a series of petal-like structures along the edge, which vary in width with radius so that if a circle is drawn at a radius r , the fraction of the circle which is blocked by petals is $A(r)$, the desired apodization function. It can be shown that the resulting electric field is then the same as that of a smooth apodization, with a series of additional perturbation terms from the scattering due to the petals. [6, 7] In our work, the occulter shape is determined using optimization methods.[6] Recent variations of our optimization approach allow modifications to enhance manufacturability or otherwise simplify the design.[8]

Our team has extensive experience designing occulter missions of various scales. In particular, we led the recent Astrophysics Strategic Mission Concept Study (ASMCS) for *THEIA*, Telescope for Habitable Exoplanets and Interstellar/Intergalactic Astronomy, a flagship 4-meter on-axis optical/UV telescope with an external occulter for planet detection and characterization.[9] The *THEIA* occulter is 40 m in diameter, with 20 petals, and is designed to work in two wavelength bands at different locations from the telescope: the 250-700 nm band at 55000 km, and the 700-1000 nm band at 35000 km. As a result of that study we were asked to present the design to the ASTRO2010 decadal survey committee and to respond to a second request for information (RFI 2) for further analysis by the committee. All of the key technologies we are proposing for development were identified as part of the ASMCS study. We have also examined the use of occulters for small scale missions using 1 to 2 m telescopes.[10] Occulters are the only technology that allows detection of Earth-like planets at that scale. In particular, we recently engaged in a study of a small scale mission, dubbed O_3 , that for reasonable cost could detect 3 to 5 Earth-like planets using a 1.1 meter telescope with an occulter and characterize them from the UV (< 300 micron) to the near infra-red (> 800 micron). The occulter we are studying here is similar to the one developed for the O_3 mission in that it allows the occulter and telescope to be compactly packaged on one launch vehicle. We have made a number of small revisions, however, to simplify this first test (see Section 2.1).

An occulter has some significant advantages over internal coronagraphs for visible-light imaging of planets: the accompanying telescope does not require the difficult wavefront sensing and control systems that coronagraphs need to compensate for aberrations in the internal optics, since most of the starlight is removed before it reaches the telescope; there is no outer working angle so the telescope can image the entire 360° region about the star at once; the shape can be chosen to make the suppression work over a broad band; and the inner working angle (IWA) of the system is largely decoupled from the size of the telescope, which allows IWA's smaller than what most coronagraphs can achieve in moderate sized telescopes (≤ 4 m).

Figure 1 shows how the *geometric inner working angle* of an occulter system depends only upon the size of the occulter and its distance. The occulter physically subtends some angular size on the sky, defining the closest angle at which a planet can be observed:

$$\text{geometric IWA} = \arctan \frac{R}{z} \approx \frac{R}{z}.$$

For objects at larger angles the occulter has little effect on the wavefront, regardless of the wavelength. It is also possible to consider imaging planets that are partially blocked by the occulter, which would effectively lower the inner working angle. However, the majority of the light from defects on the occulter will be localized within the IWA, making the tolerancing requirements of such a design considerably more difficult to achieve. Likewise, while it is possible to design an occulter mission that operates at any desired IWA with an arbitrarily small telescope, attempting to image planets inside $1.2 \lambda/D$, i.e., the main lobe of the large point spread function (PSF) of the telescope, again makes tolerancing requirements unreasonably severe.

Our recent flagship mission study, THEIA, which incorporated a 4 m telescope, was designed for an IWA of 75 mas, resulting in an occulter of 20 m radius and 55000 km distance. For the smaller O₃, which used a 1.1 m telescope, we designed an occulter with a 15 m radius and 41250 km distance giving a geometric IWA of 75 mas as well. To compare, the most ambitious coronagraph systems are hoping for an inner working angle of $2 \lambda/D$ at best; for a 1.4 m telescope over a 400-900 nm, such as proposed for PECO [11], this corresponds to 118-265 mas. ACCESS [12], which is designed for the 450-900 nm band on a 1.5 m telescope, uses a number of coronagraphs with a variety of inner working angles, with the lowest proposed at $2 \lambda/D$ as well. This would correspond to inner working angles of 124-248 mas across the band.

A second advantage of using a starshade for starlight suppression is improved throughput. The system throughput for a planet at the geometric inner working angle (90 mas for the starshade in this study) is 100% (before attenuation due to reflectivity of the optics). For closer planets (75 mas, e.g., for the TDEM starshade), where the planet light is partially obscured by the petals, the throughput drops to 50%. This is a factor of 2-4 higher than coronagraphs at their IWA. Coronagraphs typically quote the IWA as the angle where the image plane mask transmission is 50%. For bandlimited masks and visible nullers, the throughput is further reduced by the Lyot stop, again by about 50%. The Lyot stop reduction is less important for PIAA coronagraphs. Thus the bandlimited coronagraph proposed for the ACCESS mission has about 25% throughput (not including optics reflectivity) at 124 mas. Coronagraphs and nullers suffer further throughput losses because of nulls in the image plane response and the limited size of the dark hole achieved with wavefront control algorithms.

The third advantage of an occulter based mission, the broad bands allowable, comes from the fact that a single optical element creates all of the starlight suppression. In contrast, coronagraph missions have limited operational bandwidths, employ multiple optical paths over narrow bands, increasing cost and complexity, and to date cannot operate in the UV (and thus detect the ozone cutoff) because of the large number of reflections. Increasing the bandwidth of the occulter mission simply involves specifying the desired operational wavelengths in the optimization (see Section 2.1). Nevertheless, as the bandwidth is broadened, particularly further toward the infra-red, the occulter

becomes larger and the feature sizes become smaller (gaps and tips). We thus proposed for both THEIA and O₃ an occulter that operates at two distances from the telescope, each corresponding to a particular band, at the slight expense of IWA (see Section 2.1). For example, THEIA moves inward to 35000 km, which gives it a geometric IWA of 118 mas and changes its operating band from 250-700 nm to 400-1100 nm. O₃ moves in to 20625 km, for an IWA of 150 mas and operation from 500-1100 nm instead of 250-550 nm.

Despite its advantages, since the occulter acts as a diffractive optical element to provide the starlight suppression, a mission employing one has challenges of its own: the occulter has to be manufactured with great precision and retain its shape after deployment and over the course of the mission to very high accuracy; its edges must be very sharp and precisely-made to keep sunlight from being scattered into the telescope; it has to fly in very tight formation with the telescope over long distances to maintain the suppression. While some of these problems have been examined previously, none have been addressed at the scale of the occulter, e.g., meter-level formation flying over tens of thousands of kilometers. Moreover, failing to meet any one of these requirements results in mission failure; an occulter which cannot maintain shape or alignment will be unable to achieve its science objectives.

The milestone associated with this TDEM study and described in this whitepaper addresses the first of these issues—starshade petal manufacture. Our plan is to refine the petal design approach, select appropriate materials, and build a prototype petal for precision testing of the shape. Successfully accomplishing the milestone requires the use of thermal-mechanical modeling tools to determine the expected distortion in the occulter shape, and optical propagation codes for verifying performance, simulating measurements, and developing error budgets in the presence of predicted static and dynamic distortions. The remainder of this section describes our nominal design process (Section 2.1), our modeling and error budgeting process (Section 2.2), the chosen mechanical design for the occulter (Section 2.3), the current optical edge design (Section 2.4), our materials selection process (Section 2.5), and our integrated modeling tools (Section 2.6).

2.1. Occulter Design. Our approach to designing occulters uses optimization tools to determine the apodization that results in the smallest and closest possible occulter while still achieving the starlight suppression requirement over a desired wide spectral band.[6] Suppression needs to be quite deep, twelve orders of magnitude or better at the inner working angle, in order to budget for various errors in the occulter, telescope, and stationkeeping.[13] This would require a very large occulter flying quite far from the telescope (51.2 m in diameter at 70,400 km). Not only is this difficult to build and fit into a launch vehicle, the larger size and distance has significant impact on the science yield because of the time needed to transfer a larger and more distant occulter between targets. We thus placed a premium on finding the smallest possible occulter. This makes it easier to manufacture and handle, reduces the size of the launch vehicle and fairing, increases the potential science yield, and, hopefully, relaxes requirements.

Designing occulters with optimization methods first requires a model for understanding how the occulter affects light from the star. Consider a plane wave with amplitude E_0 normally incident on an occulter. Using scalar theory, it can be shown that the electric field a distance z downstream of the occulter is [6]:

$$\begin{aligned}
 E_{\text{occ}}(\rho, \phi) = & E_0 e^{ikz} \left(1 - \frac{2\pi}{i\lambda z} \int_0^R A(r) J_0 \left(\frac{2\pi r \rho}{\lambda z} \right) e^{\frac{ik}{2z}(r^2 + \rho^2)} r dr \right) \\
 (1) \quad & - E_0 e^{ikz} \sum_{j=1}^{\infty} \frac{(-1)^j k}{iz} \left(\int_0^R e^{\frac{ik}{2z}(r^2 + \rho^2)} J_{jN} \left(\frac{2\pi r \rho}{\lambda z} \right) \frac{\sin(j\pi A(r))}{j\pi} r dr \right) (2 \cos(jN(\phi - \pi/2)))
 \end{aligned}$$

where λ is the wavelength under consideration, $k = 2\pi/\lambda$, N is the number of petals on the occulter, R is the occulter radius, and (r, θ) and (ρ, ϕ) are polar coordinates at the occulter and telescope planes, respectively. The apodization function, $A(r)$, is the shape profile that defines the occulter

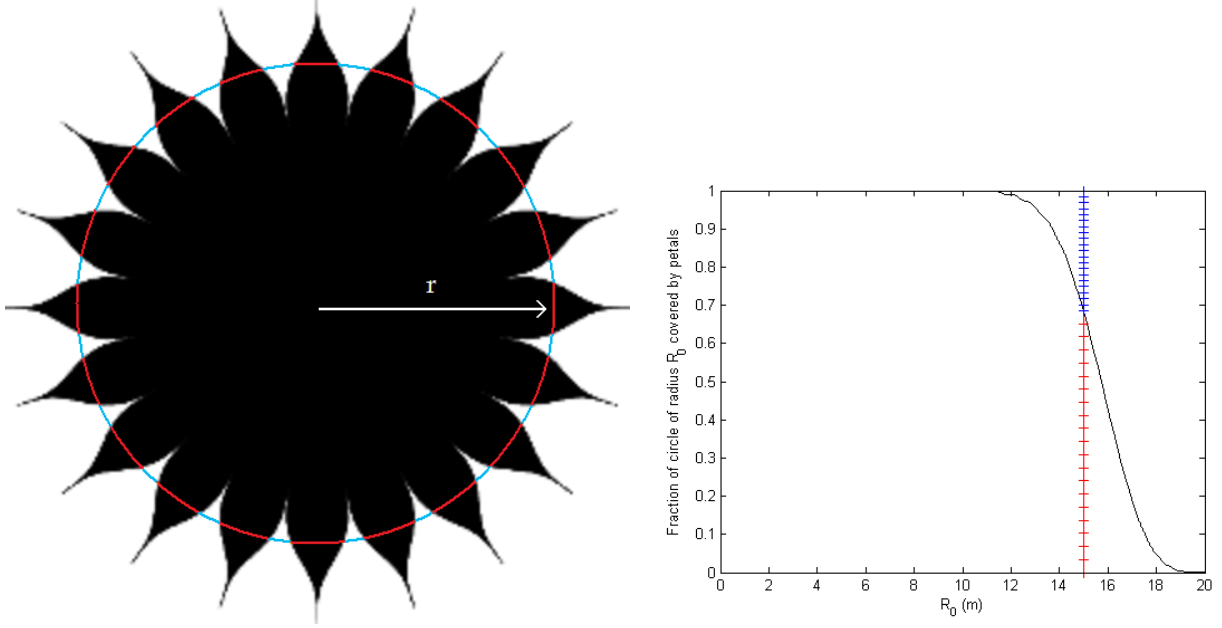


FIGURE 2. *Left.* The occulter with corresponding circle, showing the pieces blocked by the occulter. *Right.* A plot of $A(r)$ vs. r , with the segments corresponding to the lengths of the appropriate circular arcs.

and is the same as if the occulter were smoothly apodized. For a shaped occulter, it is defined so that if a circle of radius r is drawn under the occulter, the fraction blocked by the occulter is $A(r)$. (See Figure 2.)

The remaining terms in Eq. 1, comprising the infinite series, become small for small ρ when N is large. In general, when designing an occulter, we only use the first term,

$$(2) \quad E_{\text{apod}}(\rho) = E_0 e^{ikz} \left(1 - \frac{2\pi}{i\lambda z} \int_0^R A(r) J_0 \left(\frac{2\pi r \rho}{\lambda z} \right) e^{\frac{\pi i}{\lambda z} (r^2 + \rho^2)} r dr \right),$$

and select a sufficient number of petals so that the first perturbation term is negligible out to some ρ_{max} . (The magnitude of the jN -order Bessel terms will be small for $\frac{2\pi R \rho}{\lambda z} \ll N$; see Appendix A.) [7]

Given this integral representation of the pupil-plane electric field, we need to find a suitable $A(r)$; we do so via optimization. That is, we seek the apodization function $A(r)$ that minimizes the maximum bound on the electric field, c , over some shadow size and specified wavelength band subject to the constraint that the electric field everywhere in the shadow (Eq. 2) be less than the desired suppression (known as a *minimax problem*). Mathematically, the optimization problem is stated:

$$\begin{aligned}
 (3) \quad & \text{Minimize : } c \\
 & \text{subject to :} \\
 & \text{Re}(E_{\text{apod}}(\rho)) \leq c \quad \forall \quad \rho \leq \rho_{\text{max}}, \quad \lambda \in [\lambda_{\text{min}}, \lambda_{\text{max}}] \\
 & -\text{Re}(E_{\text{apod}}(\rho)) \leq c \quad \forall \quad \rho \leq \rho_{\text{max}}, \quad \lambda \in [\lambda_{\text{min}}, \lambda_{\text{max}}] \\
 & \text{Im}(E_{\text{apod}}(\rho)) \leq c \quad \forall \quad \rho \leq \rho_{\text{max}}, \quad \lambda \in [\lambda_{\text{min}}, \lambda_{\text{max}}] \\
 & -\text{Im}(E_{\text{apod}}(\rho)) \leq c \quad \forall \quad \rho \leq \rho_{\text{max}}, \quad \lambda \in [\lambda_{\text{min}}, \lambda_{\text{max}}] \\
 & A(r) = 1 \quad \forall \quad 0 \leq r \leq a \\
 & A'(r) \leq 0, \quad |A''(r)| \leq \sigma \quad \forall \quad 0 \leq r \leq R \\
 & rA(r) \frac{2\pi}{N} \geq \sigma_1 \quad \forall \quad a \leq r \leq R \\
 & r(1 - A(r)) \frac{2\pi}{N} \geq \sigma_2 \quad \forall \quad 0 \leq r \leq R
 \end{aligned}$$

Note that rather than constrain the intensity we instead constrain the real and imaginary parts of the electric field in Eq. 2. While this results in a more conservative design (by up to a factor of $\sqrt{2}$) the resulting optimization problem is a linear program which can be solved quickly and efficiently for the global minimum. We solve the linear program by converting the integral in Eq. 2 into a Riemann sum. We divide the radial extent into roughly 4000 subintervals and find the value of $A(r_k)$ at the midpoint of each subinterval, r_k , by solving the resulting linear program, where we have used the midpoint rule to convert the integral into sums. (Note that we have tried a variety of other parametric approaches using splines or various basis sets for the apodization, but all resulted in nonlinear programs that were much more complex, often didn't converge, or resulted in suboptimal occulters.)

The constraints on the apodization function itself are determined by various manufacturing and design requirements. The first two are designed to ensure the occulter has a solid central disk for the spacecraft bus and smoothly-tapering petals. (Derivatives of $A(r)$ in these constraints are approximated by finite differences between subintervals.) The final two require that the tips of the petals and gaps between petals be large enough to be manufactured. The minimum tip and gap sizes are set by σ_1 and σ_2 , respectively. This design process is iterated for different central disk sizes and different occulter-telescope distances while keeping R/z close to the desired inner working angle until the smallest occulter is found that meets the contrast requirements.

It is worth noting that while the additional terms in Eq. 1 are not used in the optimization, they *are* used to do all optical modeling after the optimization is complete, including verification of the results of the optimization. (Equivalent binary representations are also used in the error analysis, such as edge integrals or slits; see for example [13] for the methods used to perform the error budgeting.) The apodized-occulter assumption is made only in the optimization to allow it to be done as a linear optimization.

While this optimization approach is feasible and produces occulter designs that meet specifications, the resulting occulters are typically still quite large (> 50 m for a 4 m telescope) when designed for the large bandwidths we desire (nominally 250 nm to 1000 nm). One of the key advantages of occulter missions is the ability to design for wide bands, including the near-UV, enabling the ozone cutoff, with a single optical system in the telescope. However, creating suppression over such a large bandwidth typically drives the design to larger, more distant occulters, particularly as the desired science band moves into the near-IR. This motivates us to find alternate, hybrid approaches to bring down the size of the occulter. While we have investigated various approaches combining coronagraphs with an occulter in order to reduce the size of the occulter and make it easier to manufacture, none proved viable. All relied on symmetries in the propagated electric

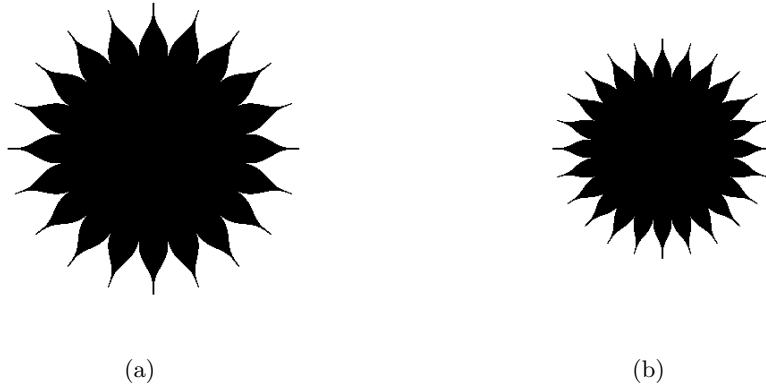


FIGURE 3. *Left.* The THEIA occulter (40 m diameter). *Right.* The O₃ occulter (30 m diameter). Both operate at distances over the bands 250-550nm and 500-1100nm.

field and thus resulted in unreasonably tight requirements on the stationkeeping. Instead, we chose to look at operational scenarios that would allow for a smaller, easier-to-manufacture occulter. Here, we took advantage of certain invariances in the Fresnel propagation integral used for occulter design.[6] In particular, we use the fact that intensity is invariant under simultaneous scalings of the wavelength and distance. That is, if we scale the distance by a constant c ($z \rightarrow zc$) and inverse scale the wavelength by the same constant ($\lambda \rightarrow \lambda/c$), then we have the same electric field (and thus shadow) at the telescope to within a phase factor, which disappears when intensity is calculated.

We thus design an occulter to operate over a band of shorter wavelengths, allowing for a smaller and easier-to-manufacture design, and then move the occulter closer to the telescope for the band of longer wavelengths. When compared to a single distance occulter, this design, for a 4 m telescope, is smaller (40 m diameter rather than 51 m), closer (55,000 km rather than 70,400 km), has significantly shorter petals (10 m rather than 19 m), and has a factor of 10 larger gaps between petals (1 mm rather than 0.1 mm). The smaller size and lighter weight shortens the slew time between observations, partially compensating for the extra time needed for characterization due to the two distances involved. Through our Monte Carlo based simulation modeling [10] we have shown that opting for the two distance design has little impact on planet detection and characterization. In addition, when using a two-distance occulter, these scaling relationships can also be used to simplify tolerancing. The image plane contrast at inner working angle R/z for the occulter at the first distance will be the same as the contrast at inner working angle $R/(zc)$ for the occulter at the second distance, allowing us to only examine tolerances based on one distance. If the requirements are met at one distance, they will work for the second distance automatically.

The THEIA and O₃ occulters are both two-distance occulters and were both designed through optimization; they are shown to relative scale in Figure 3. Note that the O₃ occulter was intentionally designed with a slightly larger number of petals (24) due to details of the kinematic design; it is 30 m tip-to-tip with 7.25 m long petals. For this study, we have modified the O₃ design to incorporate a 1.5 m telescope, thus making the image plane contrast slightly less sensitive to occulter errors and easier to fit in the facility. The resulting two-distance occulter, dubbed DI22 and shown in Figure 4, is 32 m in diameter with 6 m long petals and a slightly larger IWA, 90 mas rather than 75 mas. It operates over the same pair of wavelength bands as O₃: 250-550 nm at a distance of 36670 km and 500-1100 nm at a distance of 18335 km. We have also designed the occulter for 30 petals to lower the cost and simplify the manufacturing for this first test. With 30 petals, each petal has a width at the widest point of 2.34 m, which makes it more manageable for our existing facilities. This comes at the expense of smaller gaps between petals and narrower tips

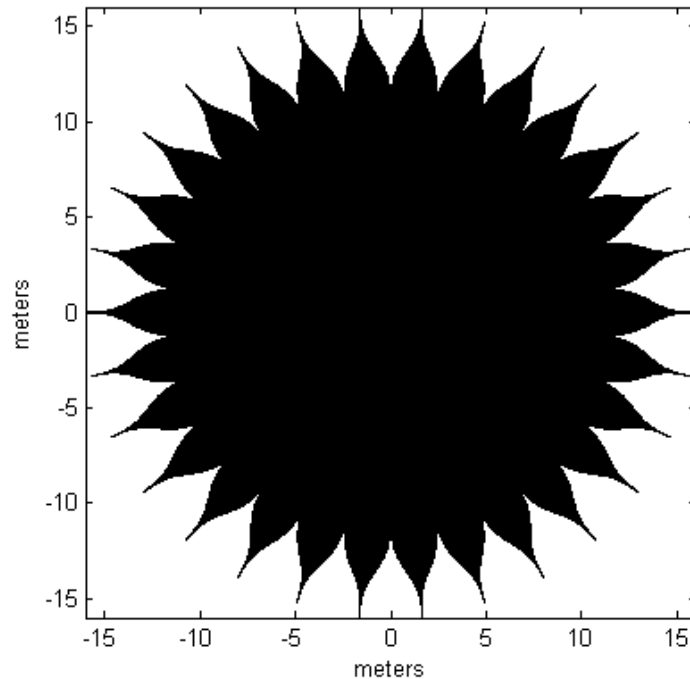


FIGURE 4. The DI22 occulter designed for a 1.5 m telescope being used for this TDEM study. It is 32 m in diameter with 30 petals, each 6 m long and 2.34 m wide at the widest point.

(1 mm). An eventual flight design would most likely have fewer, but wider, petals (as few as 16) with correspondingly larger gaps and tips (up to 2 mm).

2.2. Error Budgeting and Requirements Development. Designing the occulter through optimization is only the first step. Any realistic engineering design of the occulter can only meet the desired shape to within certain realizable tolerances. Additionally, the operation of the occulter through varying thermal environments and dynamic loading will inevitably cause variations in the shape. Our approach to developing engineering requirements on the shape and stability of the petal is via optical modeling of the field propagation from the occulter to the image plane of the telescope. It is important to base all error budgeting on image plane simulations as different errors may diffract light to different locations in the image plan and thus have more or less impact on the ability to extract a close in planet. The results of the error analysis then provide important feedback to the occulter design, to the manufacturing process, and to the selection of metrology approaches.

2.2.1. Optical Modeling. The modeling tool developed at JPL calculates the electric field at the telescope entrance aperture in two parts. First, the field for the nominal starshade design is determined using the analytic method of Vanderbei et al.[6] This solution is valid for any arbitrary distance behind the starshade that satisfies the paraxial near-field diffraction criterion. Second, the perturbations around the edges of the starshade petals and along the small inter-petal gaps are approximated as an ensemble of small slits. The width of each slit is given by the local width of the defect. The height is determined by dividing the petal length by the number of slits. Based on extensive simulations, we determined that the solution is accurately determined using 512 slits along the edge of the petal. Babinet's Principle is invoked to combine the fields of the nominal

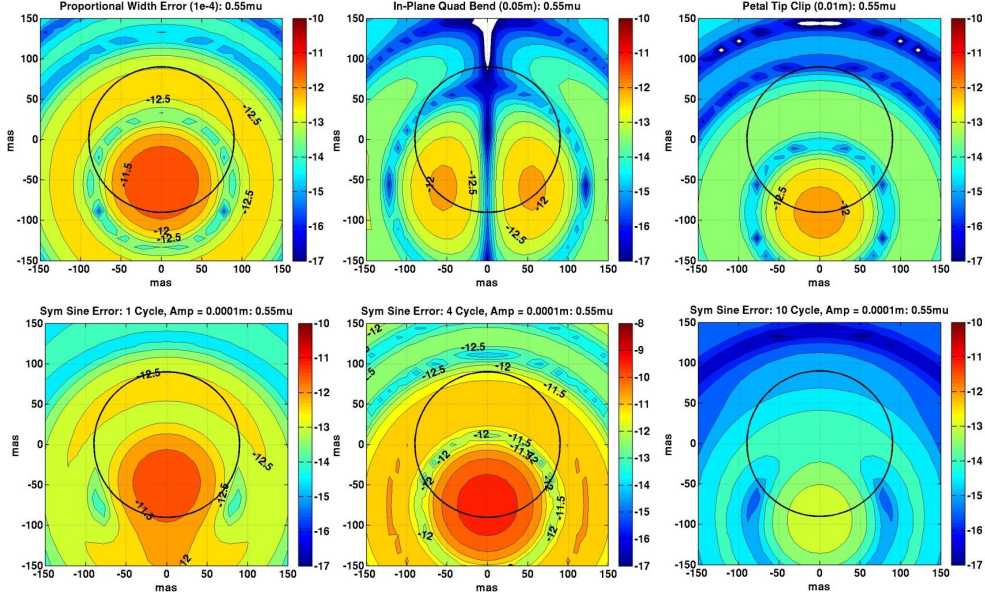


FIGURE 5. Contours of image plane contrast for six single-petal shape errors. The black circle indicates the angular geometric extent of the petals (90 mas for DI22) as seen by the telescope.

starshade and the slits: where petal edges are perturbed to block light that the nominal design passes, the field has negative amplitude. Likewise, where the petals are perturbed to pass light that is nominally blocked, the field has positive amplitude. The fields of the nominal starshade and slits are combined at the telescope entrance aperture and then propagated to the telescope image plane, again using standard techniques.

We have used this technique to model and simulate the effects of the major starshade perturbations that we expect to most severely impact performance; that is, to produce the largest degradations in contrast. Perturbations arise through petal manufacture (petal shape and installation into the starshade structure), deployment (petals go to the wrong position and can twist), thermal soak and gradients (petals bend and are displaced), and high-frequency dynamics (reaction wheels cause the petals to move). All of these have both individual petal and global (common to all petals) components that must be modeled. Based upon the modeling results for each perturbation, a global error budget is developed allocating a small amount of contrast to each perturbation such that the total mean and rms contrast is below the requirement (10^{-10} for a nominal flight mission) at the inner working angle.

Global perturbations, e.g., consistent deployment to an incorrect position, or systematic manufacturing errors common to all petals, scatter light in a circular pattern that can cause a bright spot to appear in the middle of the starshade image as well as a lumpy ring structure near the petal tips. The scatter forms a localized background field that leads to intensity cross terms that mix with the individual petal perturbations (static, thermal, and dynamic) to effectively add a homodyne boost to the perturbation scatter one would see from the individual petals. A description of the various perturbations we are considering, how they were calculated, and how they are combined can be found in [14]. Examples contour plots of image planet contrast for six different shape errors are shown in Figure 5. Outlines of four different petal shape errors are shown in Figure 6.

2.2.2. Nominal Error Budgets. The error budget and tolerancing requirements are formulated by setting a requirement on the residual contrast at the pixel containing the planet, defined as the ratio of the residual intensity in the pixels containing the peak of the planet point spread function

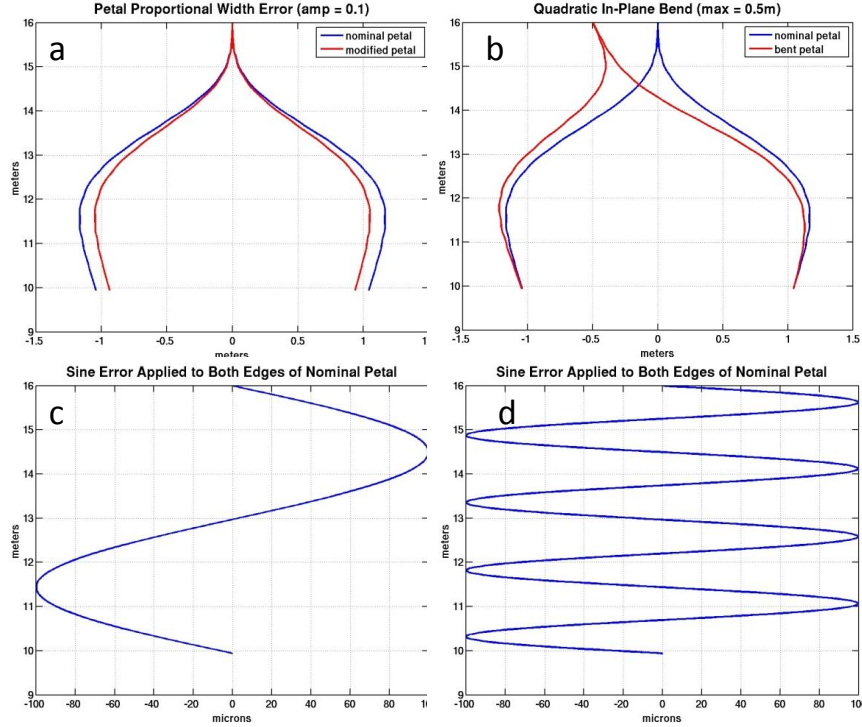


FIGURE 6. Example petal deformations. (a) Highly exaggerated proportional shape error. The minimum width error is clamped at $25 \mu\text{m}$ (not shown). (b) Highly exaggerated in-plane quadratic bend. (c) The petal edge is displaced by a 1-cycle per petal sine wave. Both sines and cosines were modeled, symmetric and anti-symmetric about the center of the petal. (d) A 4-cycle per petal sine wave error.

to the intensity in the pixels containing the peak of the stellar point spread function that would be measured with the same exposure time if the occulter were not present. The mean contrast is defined as the average intensity of background scatter (speckles) in any specified group of pixels divided by the peak intensity of the stellar point spread function that would be measured with the same exposure time if the occulter were not present. We require that the mean contrast be at the level of the zodiacal light and planet, which corresponds to a contrast of 10^{-10} . We place a tighter requirement on the rms background, that is, the variation in background intensity around the mean, to enhance the ability to distinguish a planet from background, of $\leq 10^{-11}$.

There are two possible scenarios for which we might consider performing a tolerancing analysis and developing an error budget: a spinning and non-spinning occulter. For the non-spinning occulter, petal positioning and shape defects introduce a local scatter in the image plane that is largely indistinguishable from a planet or planets (commonly referred to as *speckle*). These defects contribute roughly equally to the average and rms background level, thus making the shape and positioning requirements driven almost entirely by the 10^{-11} rms background requirement. The result is a set of extremely tight requirements on petal shape, some only a few microns.

Many of the disturbing effects of errors in the petals can be mitigated by spinning the occulter at timescales fast relative to the exposure, so that light introduced by errors is smoothed into annuli around the center of the image plane. For a perfectly-aligned occulter, this eliminates all angular variation in the intensity patterns; in the presence of lateral offset, there will still be residual structure, but at a significantly lower level. The result is a large reduction in the rms variation. In this case, the perturbation requirements are limited by the 10^{-10} mean background contrast

Perturbation	Tolerance	Units	Mean Contrast
Radial shift of petal outward (global)	0.5	mm	1.8122×10^{-11}
Proportional width (global)	40	μm per meter	1.14055×10^{-11}
4 cycle per petal symmetric (global)	6.3	μm	1.1023×10^{-11}
1 cycle per petal symmetric (global)	40.0	μm	1.0607×10^{-11}
Radial shift of petal outward (single-petal)	0.5	mm	7.93761×10^{-12}
Lateral shift of petal (single-petal)	0.4	mm	7.3902×10^{-12}
3 cycle per petal symmetric (global)	9.6	μm	5.37742×10^{-12}
Proportional width (single-petal)	40	μm per meter	4.64698×10^{-12}
4 cycle per petal symmetric (single-petal)	6.3	μm	4.50719×10^{-12}
2 cycle per petal symmetric (global)	17.7	μm	3.80017×10^{-12}

TABLE 1. Top ten contributors to occulter errors at the most sensitive wavelength ($0.55 \mu\text{m}$) for a spinning occulter, sorted by mean contrast.

wavelength (μm)	0.25	0.3	0.4	0.5	0.55
rms	9.42×10^{-13}	3.18×10^{-13}	3.67×10^{-13}	1.58×10^{-12}	4.52×10^{-12}
mean	2.45×10^{-11}	4.23×10^{-11}	6.00×10^{-11}	8.37×10^{-11}	9.86×10^{-11}

TABLE 2. Mean and rms image plane contrasts at different wavelengths for a spinning occulter.

requirement, affording a significant relaxation of requirements. Spinning also has the additional advantage of reducing thermal gradients (but the amount of thermal reduction depends on thermal time constants and the rotational speed and has yet to be modeled).

We thus adopt the spinning mode as the baseline observational scenario. While we do not discuss the engineering details associated with spinning in this white paper, our preliminary analyses have not uncovered any significant roadblocks. Spinning the occulter is feasible without overly complicating either design or operations. Nevertheless, we do not mean to imply that we find an occulter mission without spin impossible. We have completed an error analysis for a non-spinning occulter as well and should future technology and design work uncover significant challenges associated with spinning the occulter, we would revisit the error budgeting for the non-spinning case.

We have included 126 possible petal errors in our error budget. Table 1 lists the ten largest errors and corresponding tolerance requirements. These errors have been allocated according to best engineering judgement. Several of the most important terms are related to the petal attachment to the central truss and to deployment errors and can not be measured in this TDEM, which is focused on a single petal. Of the errors in Table 1, only lateral shift and radial shift terms are not addressed in this TDEM. The remaining terms are related to in-plane petal shape and scale and are either single-petal or global (common to all petals). While the TDEM does not measure global terms explicitly, measurement of a single petal bounds the global terms.

Analogously to how one might describe the shape errors in a telescope mirror, we use a polynomial expansion for the large scale deviations and harmonic terms for the mid-spatial frequencies (1-20 cycles across the length of the petal). High frequency variations will be captured through a power spectral density of the random edge errors. This breakdown of errors provides for the most convenient analytical approach to studying errors and provides important insights into the largest contributors and how they interact with the optical propagation. Nevertheless, they are not necessarily the best expansions for relating to the manufacturing process or the metrology approach. We plan to continue to refine our modeling and error budgeting process during the course

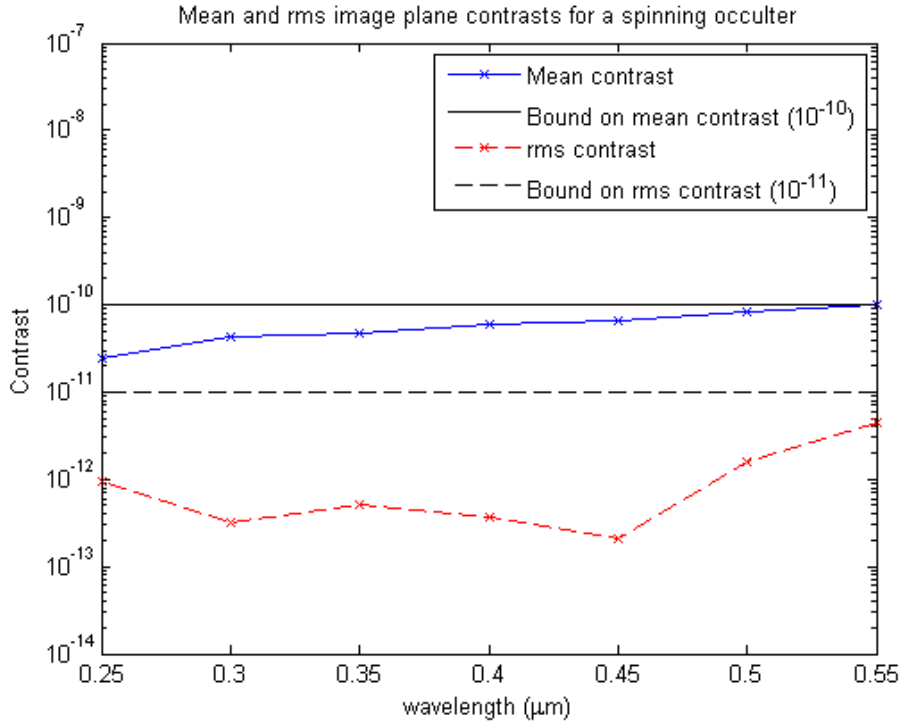


FIGURE 7. Plot of mean and rms image plane contrasts at different wavelengths for a spinning occulter.

of the TDEM with a goal to have it finalized by the start of manufacturing. These adjustments will be determined by relating measurements back to the error budget via an analysis described in Section 3.4.

The most challenging requirement is to achieve the prescribed petal shape over a narrow range of spatial frequencies that are tuned to the Fresnel Zones critical for achieving a dark shadow at the telescope. Periods of 3-5 cycles are the most critical because that is where petal edge errors are roughly in phase with the Fresnel zones that the starshade is designed to suppress. The residual contrast is also sensitive to a systematic error in the overall width of the petal as this changes the amount of light passing at any given radius and effectively alters the apodization function. Current effort is directed at defining an appropriate power spectral density for the expected high-frequency edge errors and translating that into an rms requirement on the edge shape.

Table 2 shows the total mean and rms contrast at a representative set of wavelengths for the spinning occulter. The mean contrast is the sum of the single petal speckles and the global radial terms. The rms is solely the contribution of a 1.25 m offset of the occulter with respect to the telescope-target star line of sight. Figure 7 is a plot of the values of Table 2 and the background (1e-10) and rms (1e-11) requirements.

It is important to note that all of these tolerancing requirements are representative and based on a specific occulter design and mission scenario. Further refinement and modeling is expected to occur throughout the course of the TDEM study and will be integrated with the manufacturing work and metrology specifications. We also recognize that the current error modeling was only for the occulter at the farther distance and shorter wavelengths. The next task in the error analysis is to repeat for the longest wavelength (1 μm) at the closer distance.

2.3. Mechanical Design and Manufacturing. In this section we describe our current baseline mechanical design approach. It was chosen during the O₃ study because it produces a starshade able

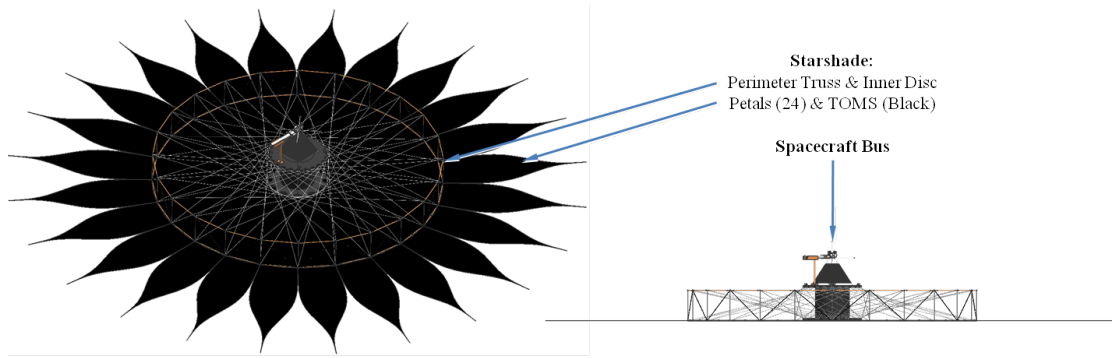


FIGURE 8. O_3 occulter and spacecraft concept showing the 30 m deployable starshade and perimeter truss.

to stow easily around the telescope and thus fit in a common fairing. While the specifics described are for the original O_3 system with 30 m starshade and 1.1 m telescope, they apply equally well to all options under consideration. In particular, the same design and manufacturing approach will be used for the 6 m nominal petal design.

A schematic of the design is shown in Figure 8. A deployable perimeter truss is used to form the inner disc and to provide a very stiff and stable interface for the petals. This design derives from the AstroMesh reflector antenna developed by Northrop Grumman Astro Aerospace (NGAS), but the opposed geodesic dome structures that normally form AstroMesh antenna surfaces have been removed. They are replaced by tensioned cords or spokes that are loosely fitted with an optically opaque blanket. The spoked structure is actually simpler and can be tuned for better stability of the rim, which is not as important for the domes when forming RF antenna surfaces.

The petals are arrayed around the circumference of the truss with only three kinematic (statically determinate) interface points: two at the base and one provided by a deployable outrigger strut (see Figure 9). The petals employ a highly mass efficient lattice structure comprised of pultruded graphite fiber reinforced plastic (GFRP) rods that have finely tuned CTEs to limit thermal deformations (see Section 2.5). The lattice structure is configured and optimized to provide stiffness and stability as required to meet petal stability requirements. All deployments are passive using stowed strain energy for actuation, dampers for rate control and separately commanded release devices for sequencing.

Both the overall structure and petal mechanical design are driven by mass and volume constraints, stiffness requirements, and the figure requirements described in Section 2.2. Applicable launch vehicles are the Atlas V and Delta-IV, both with 5m fairings that provide a usable payload envelope diameter of about 4.5m. There are numerous options for launch mass capacity within these vehicle families. Mission studies have developed conservative mass allocations for the two required spacecraft that, in combination with intermediate level launch vehicle throw capacities, lead to a starshade mass allocation of 1,000 kg. Removing reasonable allocations for the deployable truss structure, central disc and a central hub structure leaves 700 kg for the petals, which corresponds to a generous areal density of better than 2.6 kg/m^2 . The current petal prototype has an areal density of 1.5 kg/m^2 , so we view this requirement as straightforward to meet.

The first natural frequency of the occulter system (starshade and spacecraft bus) must be greater than 0.2 Hz to avoid adverse interactions with the spacecraft attitude control system. Also, the first natural frequency of individual petals, assuming a fixed base at their truss interfaces, is required to be greater than about 1 Hz to avoid coupling with occulter system modes. In practice, petal stiffness is actually driven by ground handling considerations. It is highly desirable for gravity sag strains to be a small fraction of any component elastic limit so that sag is limited to less than

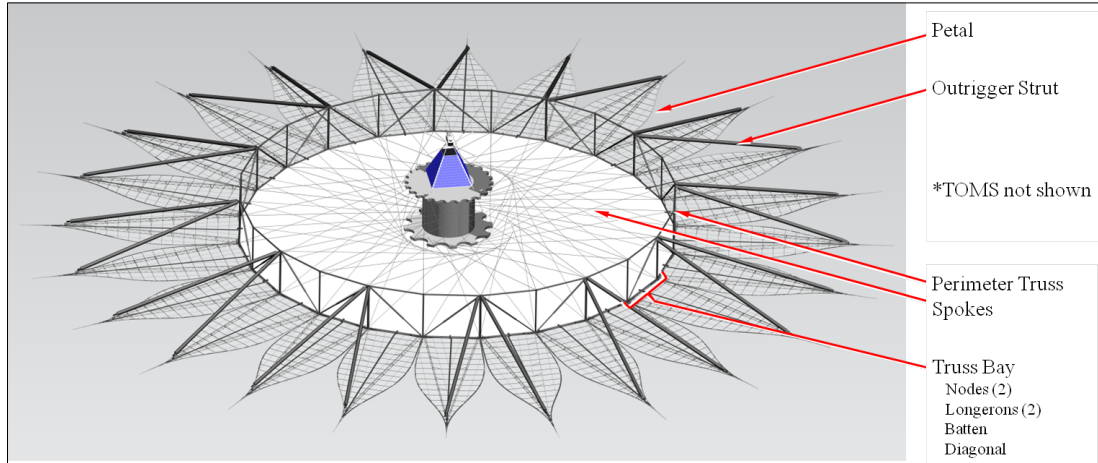


FIGURE 9. Deployed starshade.

1.5 cm. This can be achieved with very few gravity compensation fixture (GCF) offload interface points if sufficient petal stiffness is provided. It is highly desirable to minimize the number of required offload points and to locate them conveniently so that it will be possible to fully and autonomously deploy the entire starshade during ground validation and to be able to measure their alignment using advanced photogrammetry techniques.

When stowed, the starshade petals are wrapped around a fixed, lightweight central hub structure. The hub is sized to provide sufficient annular radius between its OD and the fairing ID to contain the stowed starshade truss and petals while maximizing hub diameter to reduce petal strain. For the 30m O_3 design the hub can be about 3m in diameter. The petals wrap approximately 3/4 of the way around the hub circumferentially and overlap about 2/3 of the total stowed truss height vertically.

The perimeter truss, shown in Figure 9, is a very stiff, precise and stable deployed structure. The truss rim nodes are in turn the stiff interface points from which the petals are cantilevered, with additional support provided by a deployable outrigger strut for each petal. Each petal is precisely located in-plane to maintain the global figure profile by two latches, one at each corner of the petal root. The latches provide kinematic restraint of the petal in all degrees of freedom except rotation about the axis of the truss longeron adjacent to the root of the petal. This cantilever mode of motion is restrained by the deployable outrigger strut so the flat petal bodies remain aligned with the starshade plane. The result is that the petal/outrigger combination emulates a stiff tripod for structural efficiency. This is essential for achieving a low-mass structural system with high precision.

Figure 10 shows how the petals unfurl. Deployment during the first phase is entirely passive through the controlled release of stored strain energy. Unfurling is initiated by release of a belly-band restraint system around the circumference of the stowed starshade. Lanyards that pay out from spools on passive rotary dampers and/or sequenced release devices such as pyros will meter the rate of unfurling. Once the petals are nearly straight, a pair of spring-loaded ribs pops open towards the sun-facing side of the petal to stiffen it and maintain flatness upon deployment. Deployment of the outrigger struts is concurrent with petal unfurling and is also achieved passively.

The final phase is deployment of the truss. Truss deployment is accomplished by reeling in a deployment cable on a motor-actuated spool. The cable runs around the circumference of the truss inside the telescoping diagonal members, which are extended when stowed. Spooling in the cable forces the diagonals to retract, which deploys the truss. Each bay of the truss is synchronized to



FIGURE 10. Unfurling deployment phase.

its neighbor by synchronizer gear pairs that are attached to adjacent longerons at every other truss node. The petals simply follow the truss as it deploys to complete their 90° rotation into the plane of the starshade. When truss deployment is nearly complete all petal root latch pairs engage and latch to the truss nodes. The outrigger struts also latch in place, either passively or by commanding a single latch release device ganged to all outrigger latches via a cable. While truss deployment is a critical part of the overall starshade design, the truss is not being studied as part of this TDEM.

The primary goal of this TDEM is the precision manufacturing and metrology of a single petal. Figure 11 details the petal structural design, as viewed from the telescope (anti-sun) side, with the Thermo-Optical Micrometeorite Shield (TOMS) blanket removed. The primary petal structure is a lattice of battens and longerons that intersect a longitudinal spine and a pair of structural edges on each side. These elements are optimized to place and precisely maintain the optical edge with the required profile tolerance regardless of thermal extremes or structural loads from the relatively thermally unstable TOMS. The lattice is highly mass efficient yet very stiff in-plane. Secondary petal structure includes a pair of deployable ribs in an A frame configuration that stiffen and maintain overall deployed petal flatness. The deployable ribs fold outward and flat against the petal when stowed then pop up into place when the petal is unfurling. The ribs are deployed by extension springs that are inside hollow soda-straw size GFRP struts that lock the ribs in place at a near-perpendicular angle to the petal when deployed. The ends of the deployable ribs coincide with truss-to-petal interface nodes on the base spine and with the outboard end of the outrigger at the apex of the “A” to complete the tripod-like geometry of the petal and outrigger support structure on the edge of the perimeter truss. The driver for sizing the ribs and battens is actually a 1-g petal gravity-sag displacement requirement of < 1.5 cm with the TOMS installed. This insures that a truss and petal alignment verification can be performed on the deployed starshade with high confidence prior to launch.

The battens define and maintain the precise petal edge-to-edge width. They are made from a pultruded GFRP base material that has a room-temperature axial CTE of better than $-0.2 \times 10^{-6}/^\circ\text{C}$ (see Section 2.5). The battens are continuous across the width of the petal so that joints will not affect their axial stability. To maintain edge profile tolerances, the CTE of the batten base material is designed to nominally be zero using one or more of several proven strategies that will be selected during the planned development program. (The residual error in the CTE is incorporated into our thermal-mechanical modeling. At this early stage values are based on best judgement; eventually measured CTE values will be used.)

Longerons provide the petal with in-plane shear stiffness for maintenance of the overall shape. They are made from the same pultruded GFRP as the battens, have a circular cross section and are also continuous along their length. The longest pair of longerons also act as hinge pins for the deployable ribs. Like the battens, the number and placement of longerons is somewhat arbitrary. The longitudinal and base spines provide additional stiffness and are constructed of a foam core sandwiched between thin graphite face sheets. The base spine closes out the petal root structure and carries the perimeter truss interfaces: two hinge points for the unfurling portion of deployment and two precise latches that position the deployed petal in-plane.

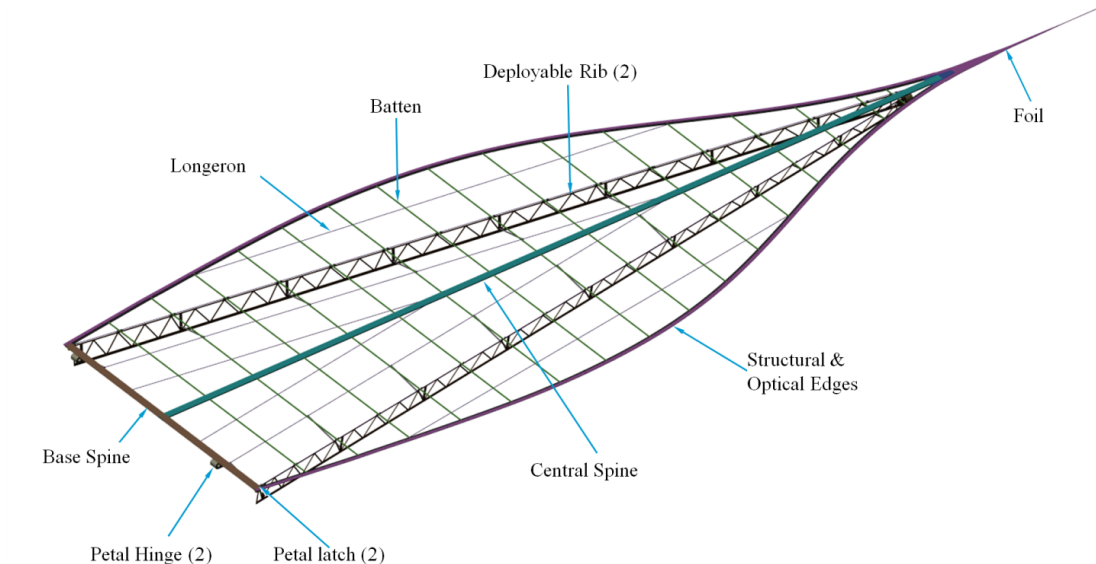


FIGURE 11. Petal mechanical design.

All petal structures are designed so that no component is subjected to more than 0.5% strain (5000 μ strain) when stowed around the 3m diameter hub. This design constraint insures that permanent plastic deformation or material creep that would degrade the deployed shape or figure of the starshade will not occur. This level of strain is only approached by the longitudinal spine in our current design, which has little or no role in the definition of the deployed petal edge profile. Its primary function is to accommodate launch restraints and deployment hardware and as a ground-handling interface. The battens are perpendicular to the direction of stowed petal strain and thus will not experience permanent set from material creep prior to launch.

The production strategy for establishing the figure profile is to first fabricate the deployable petal structure rapidly and for the lowest possible cost without utilizing high-precision tooling or metrology. This is not only to support current TDEM goals but also to minimize the cost of the ultimate flight article. The optical edges will be added later so the deployable petal structure need not be fabricated to a high degree of precision; it must simply be made of stable materials. We will use conventional low-cost composite fabrication techniques and a 8 ft range FARO Platinum 7 dof CMM with an advertised precision of $\pm 36 \mu\text{m}$ that has recently become available to us for our metrology. At this stage of assembly to FARO measurements will be made using a global reference system of tooling balls set into our ganged steel Newport tables that are in a room controlled to no better than $\pm 4^\circ\text{C}$. As a result the manufacturing tolerance for the deployable petal structure will be no better than $\pm 250 \mu\text{m}$, which is more than sufficient for the deployable structural support system.

The 25mm wide and 0.4mm thick graphite composite optical edges will be manufactured separately from the petal in the longest lengths practical for maintaining the required figure profile; between 0.8m and 1.3m long. The segments will be aligned using micrometer stages and then secured with precision clamps for a room temperature cure bonding process. A minimum number of the smallest possible bonds will be used along the length of the optical edge segments. Only enough bonding will be done to secure the edges petal for launch, deployment and operation. The petal tip is bolted into a transition plate that connects the central spine and edges together. We also note that our design iterations prior to starting manufacturing early next year includes various additional options for design, installation, and machining of the edge.



FIGURE 12. Three images of an engineering model petal before, during, and after deployment from a test fixture.

In later future development phases and for flight petals a customized laser metrology system with optical edge sensing will be used for aligning the optical edge segments on the petal structure. The metrology system will be integrally mounted on a large graphite composite bench that is in a tightly controlled environment. In addition the petals will be thermally cycled, deployed several times and their zero-g shape will be determined with photogrammetry before the optical edges are applied to insure that the petal structure has reached a stable structural state and that any as-built petal deformations that might affect the in-plane profile are removed. A validated structural finite element model (FEM) will be used to evaluate the as-built zero-gravity petal shape.

Figure 12 shows an aluminum and composite engineering model petal before, during, and after deployment from a test fixture that simulates the O₃ stowed package (all longerons and battens are made of composite carbon protruded rods while the spine and edge is aluminum). This model was manufactured to verify the design approach and confirm the kinematic performance. Since deployment is not part of this TDEM, no more deployment tests are planned during the period of performance, except for the exercising of the completed petal structure to stowed strain levels prior to optical edge integration. Nevertheless, this test model confirmed the design and will be used as a basis for manufacturing the flight-like composite petal. We also ensured that the residual strain levels (less than 0.5%) are well within the design limits of composite materials. Through the deployment of the engineering model, appropriate analysis, and coupon testing we are confident that the petal made from flight-like composite materials will meet the deployment requirements. Should time and resources allow, we do hope to perform a deployment test, but that is not part of the TDEM commitment.

2.4. Optical Edge. The occulter petals will have a separately manufactured optical edge that will be bonded to the underlying mechanical structure of the petals. The optical edge serves two functions: it is machined to the very tight tolerances that determine the width of the petals and it is beveled with a small radius of curvature to prevent scattered sunlight from entering the telescope. Both functions drive the requirements, material choices, and design.

The optical edge design is constrained by the need for a very low coefficient of thermal expansion (CTE) material to minimize variations in the edge position and the ability to manufacture an edge with a consistent edge condition that would approximate an ideally sharp edge. Carbon fiber composites have the ability to achieve a very low coefficient of thermal expansion with specially designed fiber/matrix systems in conjunction with very stringent manufacturing practices and tolerances. The manufacturing of the optical edge profile is similar for low CTE materials as well as standard off the shelf fiber/matrix systems. The profiling of the edge of a carbon fiber optical edge will affect the CTE of an engineered carbon fiber composite material. A larger bevel will have a greater affect on altering the materials local CTE. Also, as the profile gets sharper the ability to maintain a given profile becomes more difficult due to fiber size and orientations.

The mechanical design of the edge is a significant portion of the TDEM work and is a work in progress. A number of different concepts are being investigated, including tapering the carbon fiber edge, metal edges, or carbon/metal laminates. The final design will be determined based on subsection coupon tests both for machining and flexibility. The intent is develop a prototype edge from flight-like materials; questions of microcracking and deformation will be studied through sample testing, including microscope investigations of deformed longeron and edge material at Lawrence Livermore National Laboratory. Nevertheless, detailed studies of microcracking and other material properties of an installed edge during deployment are subjects of future work. Additionally, preliminary optical scatter testing is planned at the NASA Ames Research Center. This will involve measurements of scattering off various edge profile samples. This will be done on a best-effort basis as resources allow.

2.5. Materials Selection and Testing. Careful material selection is a critical part of the occulter design and verification process. The occulter structural material must be stiff and rigid when deployed yet be sufficiently flexible to roll up around the hub and deploy without plastic deformation or cracking. Of most importance is that the material have ultra-low coefficient of thermal expansion (CTE) because of the requirements for strict dimensional stability combined with the wide range of operating temperatures. The requirements described in Section 2.2 imply a needed CTE $\alpha \leq 0.15 \mu\text{strain/K}$. Any CTE less than $2 \mu\text{strain/K}$ is considered ultra-low, making this requirement challenging to meet. Adding to the challenge is that it must be maintained after the material has been stowed and deployed.

Our current plan is to use ultra-low CTE carbon fiber composites (GFRP). These materials consist of carbon (graphite) fibers embedded in a polymer resin. The small negative CTE of the graphite fibers combine with the positive CTE of the resin to give an overall CTE that can be nearly zero, tuned through the choice of the resin and how the carbon is processed. These materials are also attractive because they are strong, tough and light. They have been used previously on space missions.

We plan to conduct an assessment of various materials options for meeting the ultra-low CTE requirement, including strategies for optimization of carbon fiber composite. The key structural elements for the dimensional stability of the petal width are the battens. The initial design of the battens consists of IMF-700 carbon pultruded rods. Pultrusion is the process in which the carbon fibers are pulled through the resin prior to curing. The IMF-700 rods will be obtained from a commercial vendor. CTE measurements of the rods will be made by our collaborators at NASA Langley. We will conduct coupon tests of rods that have been bent to the radius of curvature from stowing in the occulter and then released. These tests will be performed at Lawrence Livermore National Lab (LLNL) to investigate micro-cracking. Cracking is a potential issue because the carbon fibers are brittle and even if the cracking is localized and does not lead to failure of the structural member, it can affect its properties. Electron microscopy will be used to characterize cracking in terms of crack density, location and morphology. We will investigate the implications of possible cracking on the performance including how the cracking affects material properties including CTE. The accumulation of cracking in multiple stowing/deployment sequences is also of interest. Additionally, one approach to the tuning of CTE is the use of coating layers. If this approach is needed and proves promising, we will investigate the robustness of coatings during deployment and thermal cycling both theoretically and experimentally.

Finally, electrostatic charging is an issue for all spacecraft. The poor electrical conductivity of composite materials can exacerbate local charging, leading to electrostatic discharge events. Carbon fiber composites are significantly less electrically conductive than metals. One solution used in the past has been graphite epoxy composite with embedded ASTROSTRIKE microgrid expanded metal foil (Astrodeal Products, Chester Conn.). The pure copper or aluminum foil is perforated and expanded to improve its formability and adhesion. Embedding the foil in the

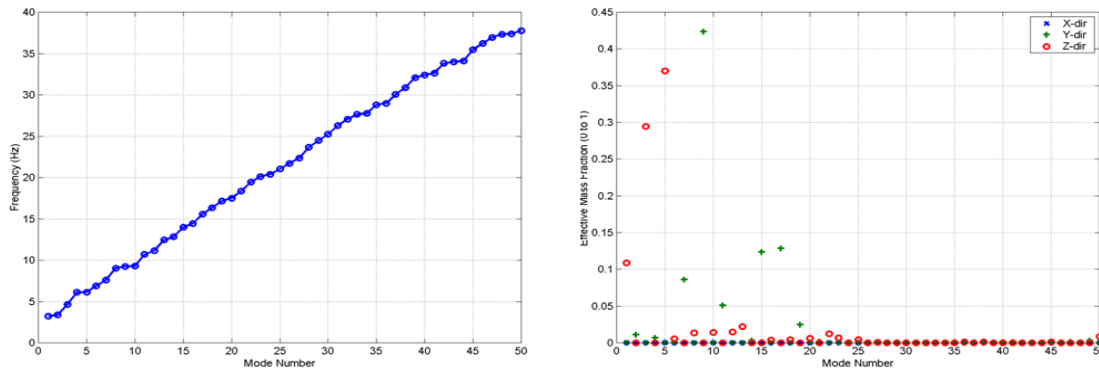


FIGURE 13. Petal FEM normal mode frequencies and effective mass fraction.

composite results in a homogeneous ground plane that minimizes noise generated from structure currents and mitigates electrostatic charge buildup. While mitigation of charging is certainly an issue, design solutions are outside the scope of this TDEM.

2.6. Integrated Modeling. In addition to the error analysis for a fixed occulter shape (see Section 2.2), it is also necessary to study the deformations in the occulter during operation to confirm that the resulting diffracted field still meets the requirements and thus that the baseline design is adequate. These deformations occur due to vibrations and varying thermal loading. Verifying the thermal and dynamic performance of the occulter, either by modeling or test, is not part of this milestone. Rather, developing the tools for such an analysis is an important part of the work necessary to converge on a mechanically adequate design with appropriate materials and thermal properties. Verification of thermal and dynamic performance based on as-built measurements and structural models is outside the scope of this milestone.

The approach we take here is to integrate structural dynamic modeling with the optical propagation tools. Results of this analysis on the nominal mechanical design are then used to iterate the design and materials selection until adequate performance is obtained. We thus confirm that the baseline design does meet the allocated deformation requirements to thermal/dynamic effects in the error budget. This section describes the modeling tools we employ.

2.6.1. Structural Analysis. NASTRAN is being used for most of the finite element modeling (FEM) work. ABAQUS has also been used for some of the large-deflection nonlinear petal component deployment analysis. Petal components are modeled using a combination of plate, solid and beam elements with composite properties as appropriate. All degrees of freedom for mechanical details of the structure are also modeled, such as in the rib hinges, which are equivalent to somewhat loose and sparsely pinned piano-hinges.

The original 7.25m long O_3 petal has a FEM mesh with 848 nodes and 1190 elements. Figure 13 shows a plot of the petal normal mode frequencies and modal effective mass fractions for the petal constrained at 3 points. Figure 14 shows a plot of the mode-shape (arbitrary amplitude) for the 1st mode at 3.2Hz. Since optical performance of the occulter is most affected by in-plane motion of the petal, modes with large effective mass in the X and Y directions would indicate significance. Such a mode is not seen until well over 5 Hz.

The FEM model for the entire occulter system was created by duplicating the detailed petal component model 24 times and attaching them with representative fitting elements to a perimeter-truss. Outrigger-struts connect the other end of the perimeter-truss to the petals at points near their rib-rib intersections. Pre-tensioned cables are used as spokes connecting the hub and occulter spacecraft bus to the perimeter-truss. The current analysis results do not include geometric/differential

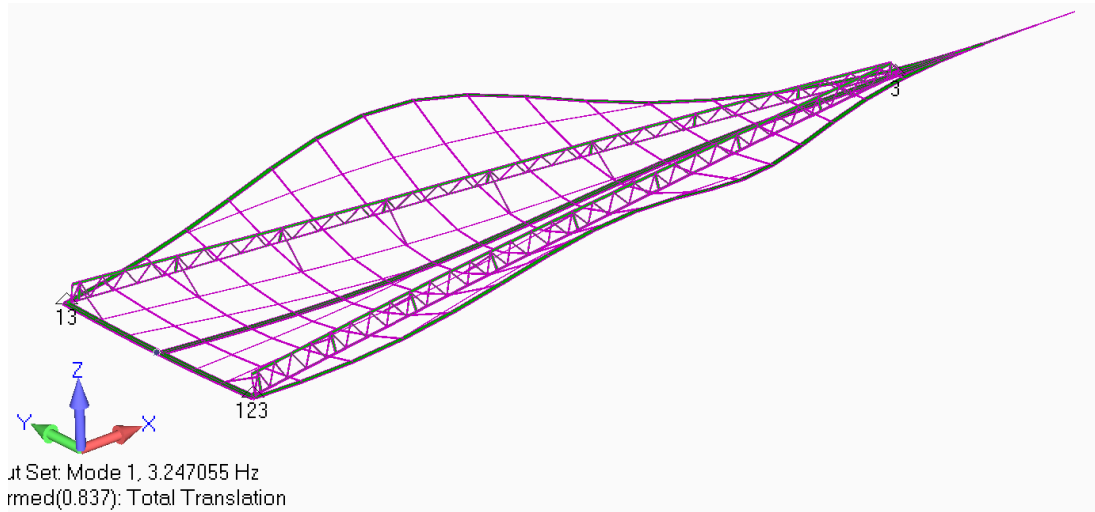


FIGURE 14. Petal 1st mode (3.2 Hz) mode-shape.

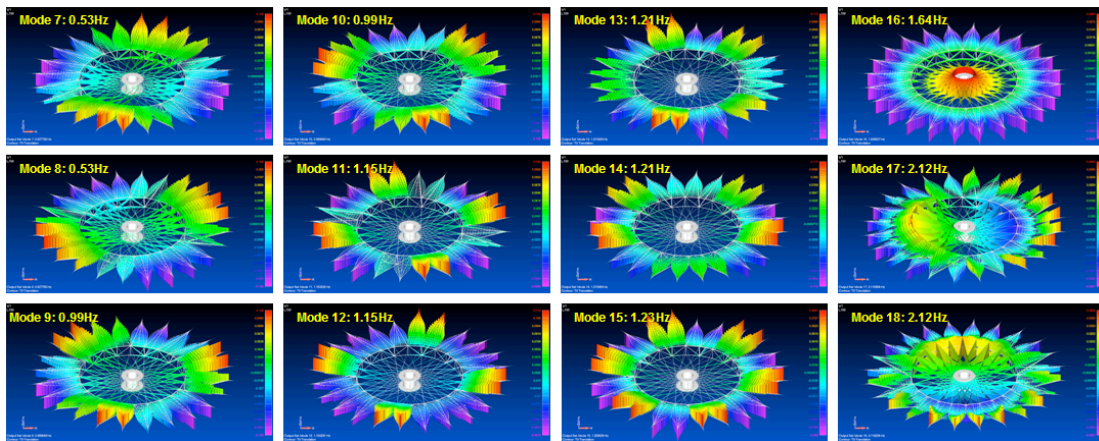


FIGURE 15. Occulter system normal frequencies and shapes.

stiffening effects of the cables; these will be analyzed using NASTRANs nonlinear analysis at a later date.

Figure 15 shows the occulter normal mode frequencies and mode-shapes for the first 12 elastic modes. The 1st mode frequency is 0.52Hz which meets our goal of 0.5Hz. We can see from the mode-shapes that the petals act as rigid bodies on the edge of the more flexible truss for these first 12 elastic modes since they are below the first petal mode of 3.2 Hz. These system modes display a similarity to Zernike circular polynomials. The mode-shapes of modes 7 & 8 (the 1st two elastic modes) are analogous to astigmatism, modes 9 & 10 to trefoil, modes 11 & 12 to quadrafoil, modes 13 & 14 to pentafoil and mode 15 to hexafoil. Mode 16 is a plunge mode analogous to power and modes 17 & 18 are analogous to coma. It should be noted that even though these mode-shapes are dominated by out-of-plane motions of the petals, the actual modal response levels were quite small for the transient excitation analyses studied.

Some mission options require the occulter spacecraft to maintain alignment with the telescope line of sight by providing lateral station keeping. We have evaluated the dynamic response to firing

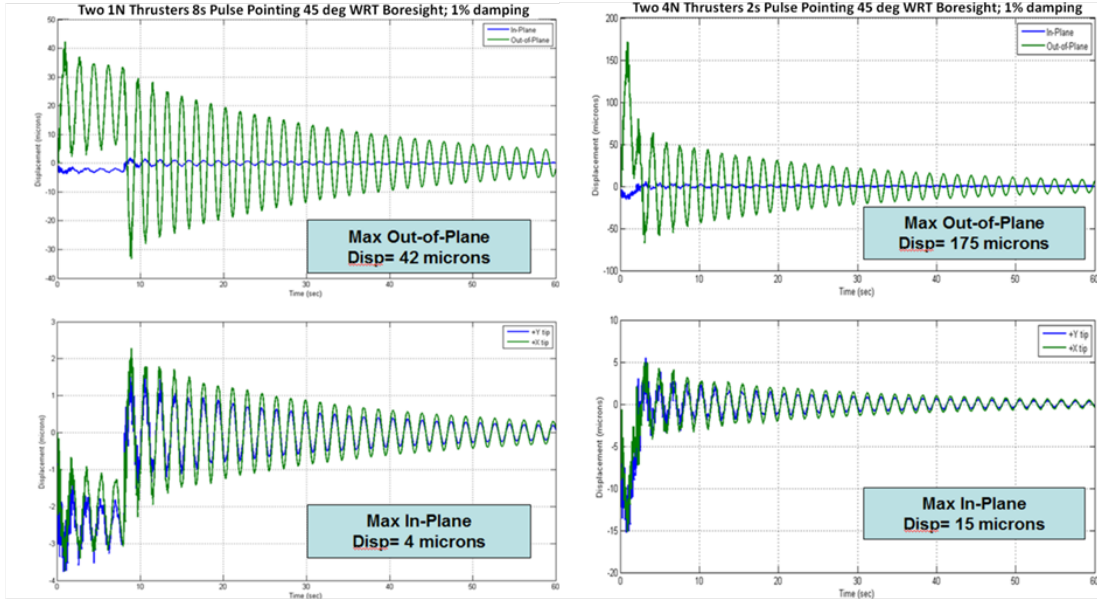


FIGURE 16. Occulter system transient response to thruster firings.

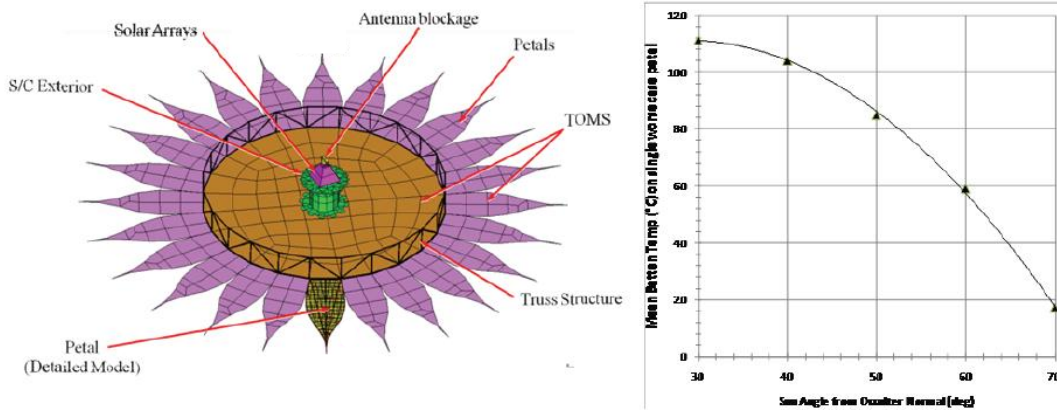


FIGURE 17. Occulter thermal model (Left) and Batten temperature vs. sun angle to surface normal (Right).

thrusters for this purpose. Figure 16 shows occulter transient response to thruster pulses of 1N for 8s and 4N for 2s respectively. Uniform modal damping of 1% was used for these analyses and experience indicates this is a reasonable guess until damping can be evaluated. The resulting in plane perturbations are limited to about 15 μm and this damps out within about 30 seconds. We have also studied the effect of scaling the occulter up by a factor of 2. The first mode dropped by an inverse ratio, but was restored over 0.5Hz by simply doubling the spoke stiffness.

2.6.2. *Thermal Analysis.* The O₃ occulter system, including spacecraft truss, and all 24 petals, has been thermally modeled using IDEAS-TMG. The mesh is shown on the left in Figure 17. Spacecraft, perimeter truss and local petal geometries are critical for capturing shadowing effects and are thus included in the model.

The key thermal issue associated with petal deformation is the deviation of batten temperatures from room temperature as sun angles change during and between science observations (as the petal was designed to achieve its nominal shape at room temperature). Thermal strains in the battens are the primary source of on-orbit petal profile errors. With a batten CTE of $-0.2\text{E-}6/\text{°C}$ and the specification of $2.0\text{E-}5$ 1-sigma proportional width error, an average temperature excursion of 100°C for all petals simultaneously would consume the entire deformation budget. Figure 17 shows a representative case for a single batten temperature as a function of solar inclination angle, as measured from occulter normal. This angle is equivalent to the Sun-target angle. Our reference mission operates with solar inclination angles between 30 and 70 degrees. Figure 17 shows that batten temperatures stay within the 100°C limit. Note that this is not an optimized design and by adjusting blanket thermal properties the temperature range can be better centered around room temperature, creating extra margin. For alternate missions with different solar inclination angles, the blanket design will be altered and the occulter will be tilted slightly relative to the telescope line of sight, creating a slightly elliptically shaped shadow and the occulter would be sized accordingly.

3. MILESTONE DESCRIPTION

3.1. Milestone Definition. Because of the early stage of occulter development, we are deliberately modest in our objectives. Our goal is to show that a precision petal can be manufactured to meet the shape requirements described in Section 2.2. A precision optical edge serves to both determine the final optical width of the petal as well as to ensure solar scattering is minimized. While the scattering properties of the optical edge are important, and we intend to do preliminary best effort measurements of optical scatter from composite edge coupons at NASA Ames, committing to specific metrology is not part of this milestone.

Our final verification will be a modeled prediction of contrast based on the measured shape of the petal:

TDEM Occulter Milestone:

- On a single full-scale petal made of flight-like materials, measure the edge position relative to a fiducial origin at a sufficient number of locations along the edge. Using our optical modeling tools, verify that the predicted mean contrast in the image plane from a uniform field propagated past an occulter with petals of the measured shape in an annulus of width equal to the full-width half-max of the telescope point spread function at the smallest inner working angle is 3×10^{-10} or better, the allocated contrast to static errors. Repeat the measurements and analysis a sufficient number of times to give 95% confidence that the predicted contrast is correct.

3.2. Summary of Requirements. Table 1 lists the top ten contributors to the occulter error budget. That is, perturbations in these categories above the tolerancing level result in errors that sum (in intensity) to larger than our overall contrast requirement. We recognize that a more careful simulation would simultaneously include all errors and account for possible couplings and cross terms as well as interactions with non-manufacturing effects, such as dynamic and thermal effects or deployment errors. Such a more detailed flow-down is valuable and will certainly be part of future studies, but is beyond the scope of this TDEM. Rather, we take the conservative approach of summing computing the effect of each error term separately and summing in intensity. We therefore set as our goal that petal perturbations in each category meet the budgeted level.

We are also focusing on only a subset of critical requirements: the proportional width error, petal in-plane bend, the first 5 critical spatial frequencies, and the power spectral density (PSD) for manufacturing the edge. The other errors in the error budget are not applicable to this set

Perturbation	Requirement	Units	Mean Contrast
Proportional Width	0.0001	n/a	1.0E-10
Tip Clip	15	mm	4.2E-11
In-plane quadratic bend	20	mm	1.4E-12
1 cycle per petal symmetric	141.4	um	5.3E-11
2 cycle per petal symmetric	50.0	um	1.6E-11
3 cycle per petal symmetric	27.2	um	3.0E-11
4 cycle per petal symmetric	17.7	um	6.2E-11
5 cycle per petal symmetric	12.6	um	6.8E-12
Symmetric residual > 5 cycles	24.7	um	5.0E-13

TABLE 3. Requirements on petal shape and corresponding allocation for the DI22 petal and a total residual contrast of 10^{-9} with an allocation to these errors of 3×10^{-10} .

of measurements. Radial offsets, lateral offsets, and in-plane rotations of the petal are measured with respect to an underlying truss; global errors and elliptical truss deformation require more of the occulter to be built in order to be explicitly tested; alignment and tilt errors affect the full starshade and require a telescope to align to; and the mechanical setup is not equipped to detect out-of-plane deformations. Tip clipping can be estimated independently of the others by simply taking one additional measurement with the arm at the petal tip.

Table 3 lists the requirements, as we currently understand them, that we seek to satisfy in the manufacture and measurement of the petal and that will be used in the assembly process. They are derived from the error budget in Section 2.2.2 but for a relaxed overall contrast of 10^{-9} . All values are a combination of global and single-petal, 1σ errors, giving equal allocation to each. For the harmonic errors, only the symmetric error requirements are listed; the anti-symmetric requirements are the same. These requirements specify the amplitude of sine-wave errors from 1-5 cycles along the length of the petal. For the remaining high frequency errors (variations > 5 cycles) we specify the maximum allowable rms residual integrated over all spatial frequencies. As we seeking a total mean contrast due to all sources of $< 10^{-9}$ for this milestone, we allocated 3×10^{-10} to the static petal shape. The remainder is allocated to deployment errors and thermal/dynamic distortion (5×10^{-10}). Thus, if all requirements are met, we expect resulting total mean contrast to be $\leq 10^{-9}$. Contrasts here were computed for a wavelength of $\lambda = 550$ nm. During the study we plan to repeat the analysis for $\lambda = 1$ μm .

The remainder of this section describes our metrology process for measuring the edge shape and our approach to analyzing the resulting data.

3.3. Precision Edge Metrology. We have considered several approaches to measuring the petal shape, keeping in mind that the edge must be measured throughout construction. Any method must achieve the desired accuracy of better than 25 μm while achieving better than 10 μm in the critical mid-spatial scales of 1.5 to 2 m. At the longest spatial scales measurement accuracy is likely to be dominated by positioning of the instrument rather than intrinsic metrology errors; nevertheless, the requirement is still determined by the sensitivity to proportional width error and accuracy must remain better than 25 μm .

Photogrammetry is one approach that would easily meet the long-range requirements and may meet the other requirements as well. This approach will ultimately be used to measure starshade deployment accuracy. However, it requires targets with contrast that stands out from the background; this is not easy to do with an optical edge that is narrow and dark. (The edge is required to have low reflectivity to reduce the scatter from Earth-shine at L2).



FIGURE 18. The Faro Platinum articulating arm coordinate measuring machine with arm length of 4 ft (1.23 m).

Laser metrology was also considered as it offers the highest precision (sub-micron distance is readily available) but these devices are either limited by angular resolution (articulating laser heads) or they require precision rails or other custom mounts. This may ultimately be used in a flight system but is beyond the available resources of the TDEM work.

We have selected an articulating arm coordinate measuring machine to measure the shape of the petal during and after construction. JPL has a 4 ft FaroArm Platinum model CMM (Figure 18) that spans the width of the petal. Because the petal is 7.25 m long, we will transfer the position of the CMM along the petal length (Figure 19) using a standard procedure that is executed in about 10 minutes. This procedure involves placing three precision spherical balls on the bench and measuring them at several points on the surface. The CMM then calculates the center of each sphere and determines the position of the base relative to the spheres. We then move the CMM to a new position and remeasure the balls. The calculations are repeated and the coordinate system is updated to reflect the new position of the base. This allows us to record measurements in one common coordinate system with origin at the initial base position for all positions of the base petal. The loss of accuracy as we move the base is related to the sphericity of the balls (a small term) and systematic errors in the measurement of their position. As a result we can perform the bonding and adjustment in sections with only minimal (few micron) loss of accuracy, well below the tolerances for overall petal shape. Section 3.4 describes how these cartesian measurements are transferred to a coordinate system located at the center of the starshade and converted to polar coordinates with the appropriate change in accuracy.

FaroArm literature specifies that the accuracy of the device, defined as worst case error within the 4 foot radius, is $\pm 36 \mu\text{m}$. This is maintained over a temperature range of 10-40 C for room temperature gradient of less than 3.5 C/minute. Assuming the $36 \mu\text{m}$ error is equivalent to a three-sigma error, the one sigma accuracy is roughly $12 \mu\text{m}$. This is consistent with the tightest requirement on the starshade, namely the one-sigma edge error for spatial frequencies ≥ 4 cycles/petal and higher of $< 13 \mu\text{m}$. The accuracy far exceeds the requirements at lower spatial frequencies.

The FaroArm precision is specified to be within $\pm 25 \mu\text{m}$, or about $8 \mu\text{m}$ one-sigma. This value can be further reduced by making multiple measurements of the petal edge. We thus expect that our final results will be limited by the device accuracy rather than individual measurement precision.

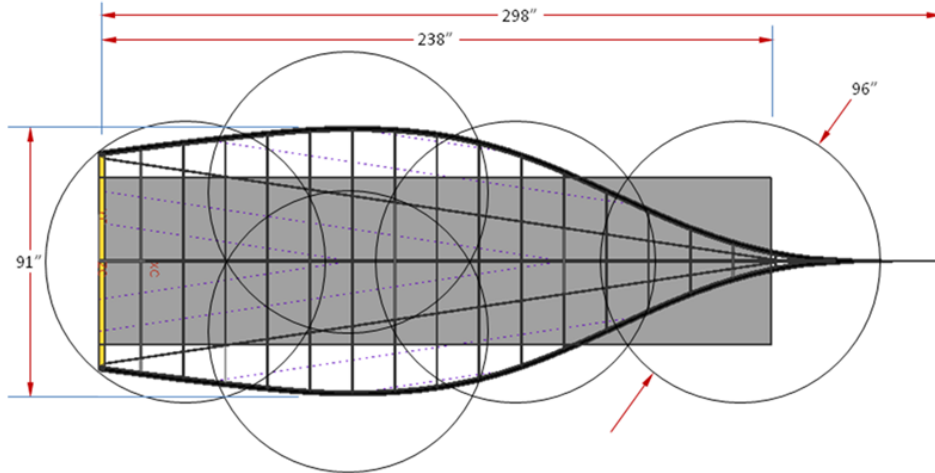


FIGURE 19. The Faro is repositioned to reach all regions of the petal. The petal tip width is measured separately using calipers as its radial and azimuthal position is not critical (at the 1 mm level) and does not require the CMM for installation.

If the existing arm does not perform to its specifications, we have a smaller (2 ft) more accurate arm available that can be used to verify the performance at spatial periods of roughly 1 m and smaller. This device has about 2x the precision and accuracy of the 4 ft arm and will be employed as necessary.

3.4. Measurement Analysis Approach. Developing a process for analyzing the measured points, transforming them, and determining whether the requirements in Table 3 were met is an ongoing one and a critical part of the funded TDEM study. It will involve a combination of fast Fourier transforms (FFTs) and fitting and careful analysis of the CMM errors. This section describes our initial progress on developing the analysis approach.

To convert the (x, y) coordinates from the measurement device into numbers for the error budget, we first transform these coordinates to radial distance and arclength (r, s) , and subtract them from the nominal shape to get a set of deviations from the nominal width. The ratio of these deviations to the nominal width gives the proportional width error, and the bending properties can be ascertained by fitting polynomials to the difference between the centerlines of the desired and manufactured petals. The power spectral density (PSD) of manufacturing errors can be determined by least-squares analysis on the residuals.

3.4.1. Defining the Deviations. We assume that the machine returns data from $2m$ locations, m on each side of the petal, giving for each measurement an x -coordinate, a y -coordinate, and errors σ_x and σ_y which are assumed uncorrelated. These measurement errors must be assigned *a priori*, based on knowledge of the variance in measurements taken with the metrology equipment, and are assumed to be small enough that the use of first-order terms in the error propagation equations is sufficient. (If these errors cannot be estimated, the following analysis may have to be rerun in simulation for a number of variance estimates, in order to see if our error estimates are usable.)

The measurement points will run the length of the manufactured occulter petal. Through an appropriate offset, the origin of the measured data is transferred to coincide with the center of the occulter. The petal is assumed to be one of N petals which make up the outer edge of the occulter. A representative set of measurement points, using a petal from the O₃ occulter, is shown in Figure 20(a).

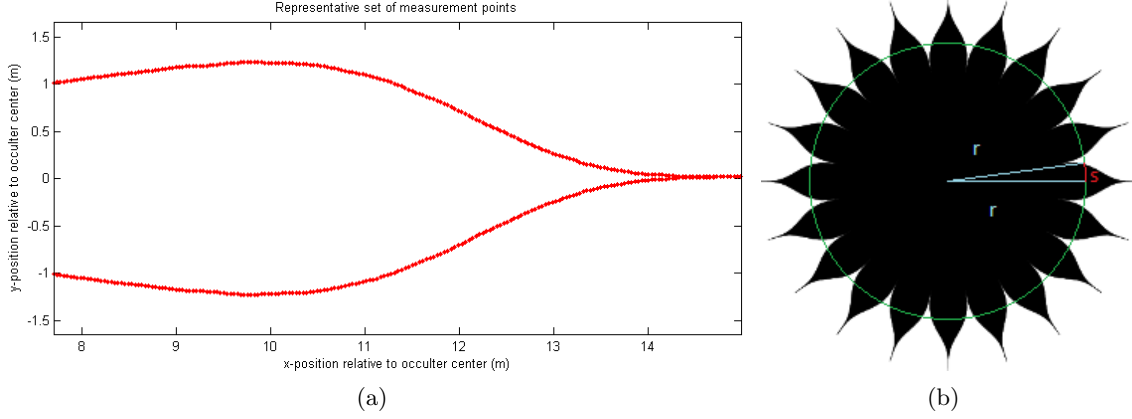


FIGURE 20. (a) 200 representative measurement points on each side of a petal from the O_3 occulter. The coordinate system is aligned to place the origin at the occulter's center and the petal centerline along the x-axis. $12 \mu\text{m}$ error bars are present on all points, though not visible due to the difference in length scales. (b) The definitions of radius and arclength; these are chosen to correspond to the way that edge errors are applied in the optical simulations that underlie the error budget.

We first convert these points into polar coordinates (r, θ) using:

$$\begin{aligned} x &= r \cos \theta \\ y &= r \sin \theta \\ r &= \sqrt{x^2 + y^2} \\ \theta &= \tan^{-1} \left(\frac{y}{x} \right). \end{aligned}$$

We estimate the variance in these new coordinates:

$$\begin{aligned} \sigma_r^2 &\equiv \sigma_x^2 \left(\frac{\partial r}{\partial x} \right)^2 + \sigma_y^2 \left(\frac{\partial r}{\partial y} \right)^2 \\ &= \sigma_x^2 \frac{x^2}{r^2} + \sigma_y^2 \frac{y^2}{r^2} = \sigma_x^2 \cos^2 \theta + \sigma_y^2 \sin^2 \theta \\ \sigma_\theta^2 &\equiv \sigma_x^2 \left(\frac{\partial \theta}{\partial x} \right)^2 + \sigma_y^2 \left(\frac{\partial \theta}{\partial y} \right)^2 \\ &= \sigma_x^2 \frac{y^2}{r^4} + \sigma_y^2 \frac{x^2}{r^4} = \sigma_x^2 \frac{\sin^2 \theta}{r^2} + \sigma_y^2 \frac{\cos^2 \theta}{r^2}. \end{aligned}$$

We assume that the center line of the nominal occulter shape occurs at $y = 0$; if not, this can be corrected by applying an offset to the angle θ . We can then convert angle to arclength subtended from center to edge at radius r , as the arclength corresponds to the set errors being applied to in

the optical tolerancing code (see Figure 20(b)):

$$\begin{aligned}
 s &= r\theta \\
 \sigma_s^2 &\equiv \sigma_r^2 \left(\frac{\partial s}{\partial r} \right)^2 + \sigma_\theta^2 \left(\frac{\partial s}{\partial \theta} \right)^2 \\
 &= \left[\sigma_x^2 \frac{x^2}{r^2} + \sigma_y^2 \frac{y^2}{r^2} \right] \theta^2 + \left[\sigma_x^2 \frac{y^2}{r^4} + \sigma_y^2 \frac{x^2}{r^4} \right] r^2 \\
 &= \left[\sigma_x^2 (\theta^2 \cos^2 \theta + \sin^2 \theta) + \sigma_y^2 (\theta^2 \sin^2 \theta + \cos^2 \theta) \right].
 \end{aligned}$$

The nominal shape on either side of the petal centerline is given as (radius, arclength) by $(r, \pm[\pi r A(r)]/N)$, and the raw deviation is given by:

$$\begin{aligned}
 \Delta_+ &\equiv \left(s_+ - \frac{\pi r_+ A(r_+)}{N} \right) \\
 \Delta_- &\equiv \left(s_- + \frac{\pi r_- A(r_-)}{N} \right)
 \end{aligned}$$

with the positive and negative signs on Δ and s corresponding to the deviation and arclength on the side of the petal with x positive and negative, respectively, and with $\sigma_{r\pm}$ and $\sigma_{s\pm}$ defined as above.

Lastly, the measurements taken on both sides may not be spaced identically in r , which can make calculation of width errors difficult. We can augment the existing data by choosing a new set of points (r_0, s_0) which we can select from existing measurements by linear interpolation. (While this is not the only interpolation method possible, it makes error propagation straightforward.) While it would be possible to resample every point to ensure even spacing, perhaps to simplify a fast Fourier transform later for calculating the PSD, it is probably better simply to interpolate the points that are not held in common between both sides, so that the measured data is retained to the extent possible. For each new r_0 between some r_1 and r_2 , we define $\alpha = (r_0 - r_1)/(r_2 - r_1)$ such that $r_0 = r_1 + \alpha(r_2 - r_1)$, $0 \leq \alpha \leq 1$, and the arclength is:

$$\begin{aligned}
 s_0 &= s_1 + \alpha(s_2 - s_1) \\
 \sigma_{s_0}^2 &= (1 - \alpha)^2 \sigma_{s_1}^2 + \alpha^2 \sigma_{s_2}^2
 \end{aligned}$$

Δ_{\pm} values for these new points are recomputed with the exact $A(r_0)$, rather than interpolating.

3.4.2. Converting into Error Budget Terms. Now, given a set of radial points r_0 and the corresponding Δ_+ and Δ_- for each, we can convert the raw deviations into terms we can use for the error budget as described in Section 3.2: proportional width error, petal in-plane bend, mid-spatial frequency harmonic deviations, and the PSD for manufacturing at the edge. We can also classify edge errors into symmetric and antisymmetric terms; symmetric errors bulge and dip identically on both sides of the petal, while antisymmetric errors have a dip on one side of the petal everywhere there is a bulge on the other. Generally, an occulter is significantly more sensitive to symmetric errors. Moreover, these error types are independent, so additional cross-terms are unnecessary.

We define a proportional width error, ϵ_p , assuming that the entire occulter petal is wider by some constant fraction:

$$\epsilon_p = p_0 \frac{\pi r_0 A(r_0)}{N}$$

with p_0 a constant parameter. In practice, we may saturate this width error at some lower value w_0 :

$$\epsilon'_p = \begin{cases} \epsilon_p, & \epsilon_p \geq w_0 \\ w_0, & \epsilon_p < w_0 \end{cases}$$

The nonlinearity of this function is difficult to fit in a least-squares analysis; allowing for some inaccuracy near $\epsilon_p \approx w_0$, $\epsilon'_p = \epsilon_p + w_0$ could be used instead. We expect w_0 to be $\sim 25\mu\text{m}$.

Bend errors have been modeled in the error budget as quadratic functions of r with zero deviation at the petal base. As the nominal petal shape is referred to the $y = 0$ line, the petal bend is calculated by the deviation of the centerline of the petal from zero:

$$\epsilon_b = a_2(r_0 - a)^2$$

with a the radius of the inner disk of the occulter. (Using $r_0 - a$ ensures the fitted bend will be zero at the petal base.) This may be extended to constant a_0 and linear $a_1(r_0 - a)$ terms in practice, though the current error budget assumes only a quadratic bend. Proportional width is a symmetric error while petal bend is antisymmetric.

Random edge errors can be split into symmetric and antisymmetric components as well:

$$\begin{aligned}\epsilon_s &= \sum_{k=1}^{20} c_{sk} \cos\left(\frac{2\pi k(r_0 - a)}{L}\right) + s_{sk} \cos\left(\frac{2\pi k(r_0 - a)}{L}\right) \\ \epsilon_a &= \sum_{k=1}^{20} c_{ak} \cos\left(\frac{2\pi k(r_0 - a)}{L}\right) + s_{ak} \cos\left(\frac{2\pi k(r_0 - a)}{L}\right)\end{aligned}$$

with L the petal length. We retain 20 terms in the current error budget. Higher-frequency edge ripples have been found to have negligible effect on the image.

We fit errors by converting the Δ_{\pm} into symmetric and antisymmetric terms:

$$\begin{aligned}\Delta_{s0} &\equiv \frac{\Delta_{0+} - \Delta_{0-}}{2} \\ \Delta_{a0} &\equiv \frac{\Delta_{0+} + \Delta_{0-}}{2} \\ \sigma_{\Delta_{s0}}^2 &= \frac{1}{4} (\sigma_{\Delta_{0+}}^2 + \sigma_{\Delta_{0-}}^2) \\ \sigma_{\Delta_{a0}}^2 &= \frac{1}{4} (\sigma_{\Delta_{0+}}^2 + \sigma_{\Delta_{0-}}^2)\end{aligned}$$

and performing independent least-squares analyses to find the parameters p_0 , a_2 , c_k , and s_k which minimize:

$$\begin{aligned}\text{Symmetric : } & \sum_i w_{si} (\Delta_{s0} - \epsilon'_p - \epsilon_s)^2 \\ \text{Antisymmetric : } & \sum_i w_{ai} (\Delta_{a0} - \epsilon_b - \epsilon_a)^2\end{aligned}$$

where the sum is taken over all i of the data points, and the weights are $w_s = 1/\sigma_{\Delta_{s0}}^2$, $w_a = 1/\sigma_{\Delta_{a0}}^2$ at each data point i .

3.4.3. Simulation of expected performance. We can test the effectiveness of this analysis by creating sets of simulated metrology data with errors which follow the tolerances provided by the manufacturer of the metrology equipment ($1\sigma = 12\mu\text{m}$ accuracy). To do so, we create known symmetric and antisymmetric errors on both sides of the petal and measure edge points on the perturbed edges, inserting appropriate noise at each measurement. This ‘‘practice data’’ can serve as a test set for the reconstruction procedure above.

We used this simulated data on the O_3 occulter design to verify our operating procedure, generating all of the errors simultaneously at the maximum allowed extents from Table 3. Table 4 shows the exact and measured values of the proportional width and quadratic bend errors using 200 points. Figure 22 plots the fitted symmetric and antisymmetric sinusoidal errors, which were

TABLE 4. Actual and fitted proportional width and bend terms.

	Actual	Fitted
Proportional width (unitless)	7×10^{-5}	$7.01 \times 10^{-5} \pm 0.16 \times 10^{-5}$
Quadratic bend	20mm	$19.998\text{mm} \pm 3.1\mu\text{m}$

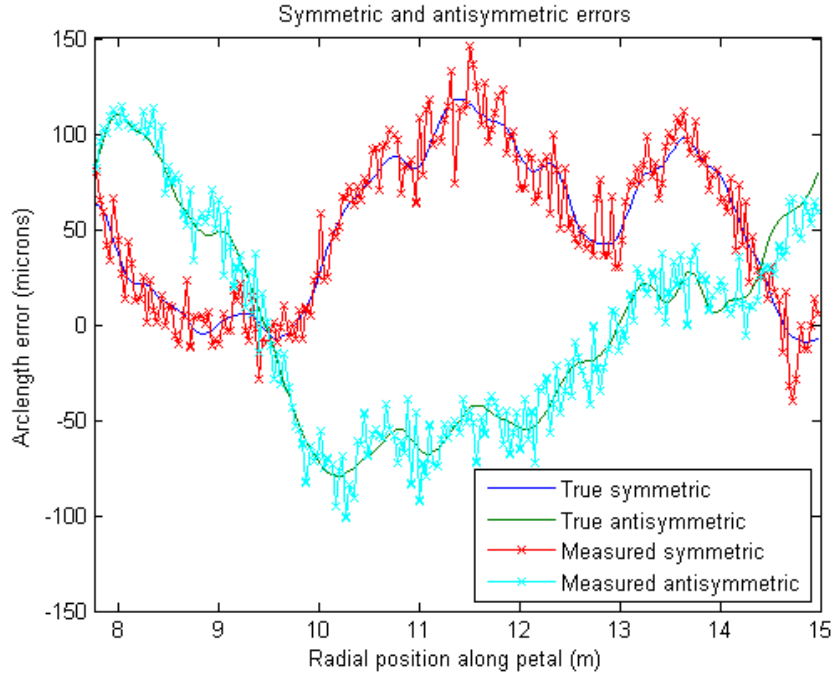


FIGURE 21. The magnitudes of sinusoidal and proportional width errors, as symmetric and antisymmetric terms

chosen randomly to satisfy the power-law underlying the requirements in Table 3. The symmetric and antisymmetric sinusoidal errors along the petal, with the proportional width error added to the symmetric term, are shown in Figure 21. Each measurement is at 200 points along the edge, and these are shown with the true deviation from nominal.

These simulations suggest that the planned methodology and hardware are able to acceptably measure the various errors the petal may be subject to, even when they near the limit of their error budget allocation.

3.5. Predicting Contrast. Ultimately, the metric that matters is contrast. Have we manufactured a petal well enough such that the resulting starlight suppression is sufficient? Our milestone addresses this question of whether an occulter composed of petals made to the same accuracy as our demonstrated one will achieve the needed contrast. Ideally, we would like a metric that determines the probability that the petals ultimately produced for flight by our manufacturing process are “good enough”, that is, would form an occulter that is guaranteed with some level of confidence to statically produce the desired image plane contrast (the question of speckle statistics over time, due to both thermal and dynamic distortion, is also an important one but outside the scope of the current study). Unfortunately, developing such a metric would require manufacturing and testing many petals to develop a statistically meaningful data set; something that is clearly beyond the funds available. This is, of course, why most satellites are so thoroughly tested before flight.

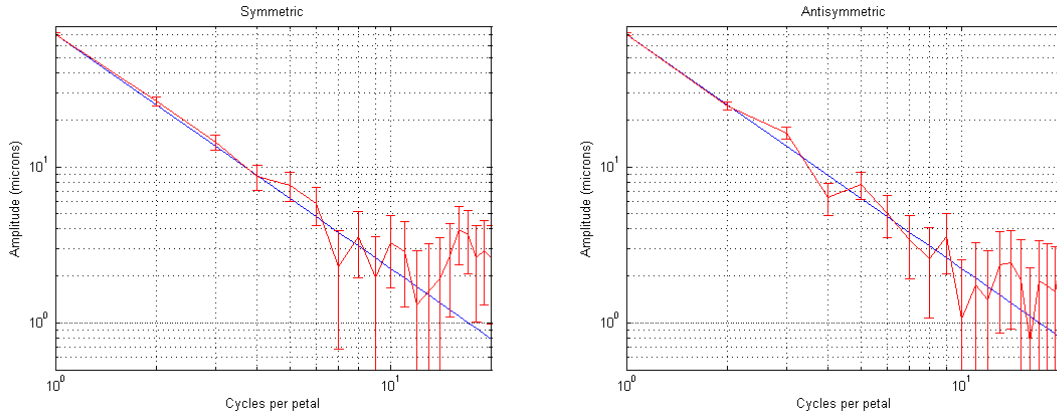


FIGURE 22. *Left.* Exact (blue) and fitted (red) amplitudes for sinusoidal symmetric errors. *Right.* Exact (blue) and fitted (red) amplitudes for sinusoidal antisymmetric errors.

We are also faced with the unfortunate problem that there is no reasonable optical test that can be done on a full scale occulter or even a single petal to directly measure the starlight suppression. While it is possible to create a reasonable laboratory facsimile of a coronagraphic system, and thus make direct measurements of contrast, that is not possible for occulter based approaches. Rather, we are forced to rely on modeling using indirect measurements (such as occulter shape) and an appropriate statistical analysis to give ourselves confidence in the design and workmanship.

For this TDEM, in our first effort to manufacture and measure an occulter petal, our objectives are modest. We are making a single occulter petal and using our measured shape to make the determination of whether *that petal* was manufactured well enough. In other words, would an occulter made up of petals identical to our single manufactured petal produce the desired contrast at the desired inner working angle? While this does not address the statistics of manufacturing petals, it does validate the design and demonstrate that the processes we developed (both manufacturing and metrology) are adequate.

The statistical problem here is associated with the measurement error and resolution, since we can't know the shape of our manufactured petal better than we can measure it and we can't know the variations in shape between measurement locations. There are two types of measurement error we need to understand and model, random (precision) and systematic (accuracy). As described above, systematic effects are reduced by using calibrated fiducial gauge blocks for calibrating the CMM. Random errors are treated statistically and reduced through repeated measurements, as described in Section 3.5.2 below.

It is useful to view the milestone in the context of hypothesis testing. Once we have completed manufacturing and measuring the petal, we perform analysis to address the hypothesis that the petal is sufficiently well made to produce a static contrast of 3×10^{-10} .² The results of the image simulation will allow us to either confirm or reject the hypothesis.

There are two types of errors one might expect. The first results in a rejection of the hypothesis (the contrast is not sufficient) despite the petal actually being manufactured well enough (Type I error). In other words, the measurement error is such that when used in our simulation we fail to achieve the desired contrast even though the underlying shape meets requirements. The second results in an acceptance of the hypothesis despite the petal not meeting requirements (Type II error). Here, the measurement error is such that it fools us into believing the petal is made better than it actually is. Our goal is to reduce the probability of both types of error to less than 5% via

²Again, for this first experiment we are not necessarily trying to reach the full flight requirement.

proper choice of metrology equipment, careful modeling, repeated measurements, and appropriate simulations. We hope for a 95% confidence that the as-built petal meets requirements and would result in an occulter, with all other deviations nulled, that produces the desired contrast.

In the remainder of this section we describe our analysis approach for using the measured data to predict contrast and the statistical analysis to ensure the desired confidence.

3.5.1. Estimating Contrast from a Set of Measured Points. Given m measurements along a petal there are, of course, an infinite number of actual petal shapes consistent with the measurements. This is analogous to the polynomial fitting problem, where one cannot fit a polynomial of higher order than the number of measurements. Nevertheless, we know that there are certain smoothness constraints that limit the variations between measurements for a real petal. Our objective is to find both a methodology for computing contrast estimates given a finite number of width measurements and a process for determining the critical number of measurements, m_c , for which we obtain the desired statistics while still remaining below a measurement number that could be reasonably accomplished in the laboratory.

Our selected approach for computing the contrast estimate is to first find the deviations, ϵ , from the nominal shape as described in Section 3.4. We can then use our available analytical tools, described below, to calculate the contrast. There are two possible ways we might generate these shape errors from measurements: (1) create a piece-wise continuous petal shape via cubic spline interpolation between the measured values and subtract the nominal shape and (2) fit the measurement residuals to a specific error model as described in Section 3.4. Approach (1) has the advantage of using only the measured points with no modeling assumptions, but may prove to require an unreasonable number of measurement points. Method (2) has the advantage that it can be done with any number of points and ties back to our earlier analysis approach, but involves a more complicated analysis and assumptions about the errors. Our final choice will be based on our determination of m_c for each and our experience taking measurements.

For the first approach, the critical number of measurements, m_c , along the two edges of the petal can be found via simulation. For some value of m , we create multiple different petal shapes consistent with m measurements along the edges and the error characteristics defined in Section 3.4. We then generate the errors for each shape by subtracting the nominal petal shape, and calculate the resulting contrast values via the algorithm described below. We repeat this procedure for increasing values of m until the variance in the resulting contrast levels is below the desired contrast. If this yields a value for m_c that corresponds to a feasible number of measurements, then the “measured” petal shape errors can be produced by simply applying cubic splines (or any other interpolant) to the measured data set and subtracting the nominal shape. If, however, the value required for m_c to constrain contrast variations to below the requirement proves to be too large, we would instead generate the petal shape errors via fitting procedures such as the ones described above in Section 3.4.

Once we have a sufficient number of interpolated values to describe the petal shape and have derived the corresponding errors on each side, we can compute the predicted contrast at the image plane for an occulter composed of identical copies of this petal. Cady [15] showed that the Bessel function formalism in Eq. 1 can be extended to determine the effects of single-petal errors. Consider modifying the profile $A(r)$ on each edge of petal n_0 to become $A(r) + \epsilon_1(r)$ and $A(r) + \epsilon_2(r)$. (As previously, we assume that there are N petals; n_0 refers to the particular petal we are looking at, with $n_0 \in 0, 1, \dots, N - 1$.) It can be shown that when errors $\epsilon_1(r)$ and $\epsilon_2(r)$ are applied to the two edges of a petal (with ϵ_1 placed on the side of increasing θ without loss of generality), we can write

the resulting electric field:

$$\begin{aligned}
 E_\epsilon(\rho, \phi) &= E_{\text{bin}}(\rho, \phi) - \frac{2\pi}{i\lambda z} \int_0^R \exp\left[\frac{\pi i}{\lambda z}(r^2 + \rho^2)\right] J_0\left(\frac{2\pi r \rho}{\lambda z}\right) \frac{1}{2N} [\epsilon_2(r) - \epsilon_1(r)] r \, dr \\
 (4) \quad &- E_0 \exp\left(\frac{2\pi i z}{\lambda}\right) \sum_{m=1}^{\infty} \frac{i^m}{i\lambda z} \left(\int_0^R \exp\left[\frac{\pi i}{\lambda z}(r^2 + \rho^2)\right] J_m\left(\frac{-2\pi r \rho}{\lambda z}\right) F_{n_0}(r, \phi) r \, dr \right) \\
 &\equiv E_{\text{bin}}(\rho, \phi) + E_{n_0}(\rho, \phi)
 \end{aligned}$$

where

$$\begin{aligned}
 F_{n_0}(r, \phi) &= \frac{2}{m} \left\{ \left[\sin\left(\frac{\pi m}{N}[A(r) + \epsilon_1(r)]\right) + \sin\left(\frac{\pi m}{N}[A(r) + \epsilon_2(r)]\right) \right. \right. \\
 &\quad \left. \left. - 2 \sin\left(\frac{\pi m}{N}A(r)\right) \right] \cos\left(m\phi - \frac{2\pi m n_0}{N}\right) \right. \\
 (5) \quad &\left. - \left[\cos\left(\frac{\pi m}{N}[A(r) + \epsilon_1(r)]\right) - \cos\left(\frac{\pi m}{N}[A(r) + \epsilon_2(r)]\right) \right] \sin\left(m\phi - \frac{2\pi m n_0}{N}\right) \right\},
 \end{aligned}$$

E_{bin} is the ideal electric field from a perfect petal and E_{n_0} is the perturbed electric field. Note that E_{bin} can be determined independently of the perturbations and saved, and the perturbation term E_{n_0} may be calculated separately. Perturbations may be switched out quickly, and more petals may be added by changing n_0 and recalculating and adding the next electric field term to E_ϵ . In this manner, we can build the electric field at the telescope pupil plane following the occulter. (As the symmetry of the occulter will be broken by edge perturbations, it will generally be necessary to retain a significant number of Bessel terms in the series in Eq. 4 to ensure the electric field is accurately calculated over the aperture.)

The profiles $\epsilon_1(r)$ and $\epsilon_2(r)$ are unitless; to convert an error with units of length $d(r)$, such as a sinusoidal error, into a form usable in Eq. 4 and Eq. 5, we use the expression:

$$(6) \quad \epsilon(r) = \frac{Nd(r)}{\pi r}$$

over the length of the petal. For proportional width error, we use $\epsilon(r) = p_0 A(r)$.

To determine the contrast resulting from an occulter based on repeated petals taking on the measurement shapes from repeated sets of measurements, we make estimates of $\epsilon_1(r)$ and $\epsilon_2(r)$ from each set of points, using either the nonlinear fitting procedure outlined for the various errors in the error budget, or by calculating the deviation of the interpolant from the nominal petal shape. At this point, we also introduce errors representative of the other error allocations in the error budget: that is, the ones that could not be tested from a single petal, such as lateral and radial offsets of petals. Eq. 4 can then be used to evaluate the electric field across the telescope aperture at wavelengths across the working bandpass of the occulter.

To calculate contrast in the image plane, we assume a representative telescope with diameter D , pupil function $P(\rho, \phi)$, and focal length f and propagate a star and planet through it. The pupil function is assumed to be a $[0, 1]$ -valued function defining the shape of the telescope aperture. For a star, which is assumed to be an on-axis source, the electric field at the image plane is given by:

$$(7) \quad E_{\text{im}}(a, \theta') = \frac{1}{i\lambda f} \int_0^{D/2} \int_0^{2\pi} E_\epsilon(\rho, \phi) P(\rho, \phi) e^{2\pi i \frac{\rho}{D} a \cos(\phi - \theta')} \rho \, d\rho \, d\phi$$

where a is the radial position in the image plane in λ/D , and θ' the angular position about the optical axis. We simulate a planet by propagating an off-axis plane wave past the occulter; [15] shows that the electric field from an off-axis source at the pupil plane is equivalent that of an on-axis source with an offset pupil location and a phase shift, so this may be done with Eq. 4 and

Eq. 7 as well. We define the IWA for an occulter as its geometric angular size on the sky,

$$(8) \quad \text{IWA} = \arctan\left(\frac{R}{z}\right) \approx \frac{R}{z},$$

and we use this angle as the off-axis angular position of the planet. The intensity c of the plane wave simulating the planet will be allowed to vary to represent a brighter or dimmer target.

Following [14], we define an annulus in the image plane centered on the star with diameter equal to this IWA and a width equivalent to the FWHM of the PSF. Within this annulus, we determine the mean intensity of the star I_s ; the peak of the planet PSF will also fall in this annulus, with a peak intensity $I_p(c)$. **We define the contrast as the value of c , the intensity of the signal from the simulated planet before the occulter, such that $I_p(c) \geq I_s$ for all wavelengths in the spectral passband of the occulter.**

3.5.2. Determining Confidence Intervals on Contrast. The question of whether a set of measurements represent a petal capable of achieving the desired level of contrast breaks down into two statistical analyses. First, we must quantify the errors on individual measurements. As described in Sections 3.5.1, we must ensure that we can map a set of measurements to a petal shape with sufficient accuracy so that any variations in petal shape consistent with both the measurements and the known measurement error results in contrast variations below the required contrast level. Once this is achieved, our second task is to find the distribution of contrast values associated with repeated trials of measuring the petal shape, and to test whether the most likely estimate for contrast meets our milestone goal.

Once the distribution of measurement errors has been established, using the CMM manufacturer's specification and independent test against known samples, we can answer the fundamental question of whether an occulter composed of petals identical to the one we have manufactured can meet the contrast requirements. We do so by establishing a confidence interval for the contrast that would be generated by this occulter, effectively testing the null hypothesis $H_0 : c < 3 \times 10^{-10}$, against the alternative $H_\alpha : c \geq 3 \times 10^{-10}$. While the distribution of contrasts will likely not be Gaussian (as it involves a non-linear mapping from a Gaussian distribution of errors), assuming it is sufficiently well sampled, the distribution of $(\bar{X} - \mu)\sqrt{n}/s$ is roughly normally distributed about zero with a standard deviation of 1, where \bar{X} is the maximum likelihood estimator (MLE) for the parameter, n is the number of samples, μ is the population mean, and s is the sample standard deviation. Furthermore, assuming a smooth distribution for contrasts, it may be possible to fit a continuous function for this distribution, making the interval estimate even more precise.

To accept our null hypothesis, we must say with some confidence α that c falls below the required contrast level, which is equivalent to calculating the probability that c falls below the lower bound of the $(1 - \alpha)$ confidence interval on contrast. If using a sufficiently sampled distribution that can be remapped to a Gaussian, this is equivalent to performing the upper-tailed z-test, with test statistic given by $Z = (\bar{X} - c_0)\sqrt{n}$, where c_0 is the contrast requirement. We thus reject H_0 in the case of $z > z_\alpha$, where z_α is the value of the standard normal variate with probability α . The associated power of this test— $(1 - \beta)$, where β is the Type II error risk—is given by

$$1 - \beta = 1 - p(z < z_\alpha - \delta^*\sqrt{n})$$

where δ^* is the difference between a contrast drawn from a distribution which fails the hypothesis test ($c > c_0$) and a contrast drawn from the null hypothesis distribution. This same power calculation can also be used to find the required sample size of measurement sets (i.e., measurement trials).

The procedure we would take would be as follows:

- (1) Determine the number of measurements, m , to be used in each trial:
 - (a) Define the measurement noise as equal to the mean CMM measurement error (determined from the manufacturer's specification and lab testing).

- (b) Simulate multiple sets of m noisy petal measurements for increasing values of m , finding the contrasts associated with cubic splines of each set, until variations between the produced contrasts fall below 3×10^{-10} .
 - (c) If this maximum value for m is feasible in laboratory testing, use this m and produce petal shape error approximations by directly comparing the ideal shape with an interpolated shape from m measurements. Otherwise, use the largest possible value for m and adopt the error-fitting procedure described in Sections 3.5.1 and 3.4.
- (2) Take n sets $\{Z\}_{i=1}^n$ of m measurements each, $Z_i = \{z_j\}_{j=1}^m$, which produce n measured petal shapes. The number of sets, n , will be determined so that the MLE for the contrast falls within the α confidence interval for the mean of the sample set.
 - (3) Apply the mapping $f : Z \rightarrow c$ described in Sections 3.5.1 to the n measurement sets to produce a distribution of contrasts.
 - (4) Using the derived distribution function for c , find the maximum likelihood estimator \bar{c} . Apply the hypothesis test $H_0 : \bar{c} \leq 3 \times 10^{-10}$, with $H_\alpha : \bar{c} > 3 \times 10^{-10}$. A failure to reject the null hypothesis at a confidence level of α represents the successful creation of a petal capable of producing the required contrast.

4. SUCCESS CRITERIA

While establishing an error budget and formulating requirements on petal shape is essential, and an integral part of our TDEM activities, the ultimate objective is to achieve sufficient starlight suppression. Our approach is there for not to provide a comprehensive comparison of the measurements to a derived error budget, but rather to set as our success criteria a confirmation of (a slightly relaxed) mean image plane contrast of 3×10^{-10} at the geometric inner working angle were a full starshade to be built to the measured accuracy of our petal with all other terms in the error budget set to zero. We will establish success using the analytical process described and the following combination of metrology and modeling:

- (1) Perform measurements of the shape of each side of the petal relative to a fiducial origin in Cartesian coordinates along each edge as described in Sections 3.3 and 3.5.2 with measurement error quantified as in Section 3.3.
- (2) Transfer the measurements to a common coordinate system and convert to polar coordinates as described in Section 3.4.
- (3) Perform a fit to confirm that the measurements fall within the range of the requirements in Table 3 from the error budget as finalized by the time of the final measurements as described in Section 3.4.
- (4) Steps 1—3 must be satisfied on three separate occasions with at least 24 hrs between the end of one set of measurements and the beginning of the next set of measurements.
- (5) Take a set of measurements and generate a set of measured errors either by fitting or by subtracting an interpolated petal shape from the nominal shape.
- (6) Using our optical modeling tool, propagate an incident plane wave past the simulated occulter to the image plane of the corresponding telescope. Repeat the monochromatic analysis for a selection of three or more wavelengths in the designed-for passbands, including the maximum and minimum design wavelengths.
- (7) Calculate the mean contrast over an annulus of width equal to the full-width half-max of the telescope point spread function at the inner working angle at each wavelength.
- (8) Repeat steps 5, 6, and 7 N times to produce N values of contrast from N measurement sets, with N determined by a statistical power test. Perform hypothesis testing as described in Section 3.5.2 to determine whether a starshade composed of copies of the manufactured petal would provide $\leq 3 \times 10^{-10}$ contrast at the inner working angle across the passband.

5. CERTIFICATION

The PI will assemble a milestone certification data package for review by the ExEPTAC and the ExEP program. In the event of a consensus determination that the success criteria have been met, the project will submit the findings of the review board, together with the certification data package, to NASA HQ for official certification of milestone compliance. In the event of a disagreement between the ExEP project and the ExEPTAC, NASA HQ will determine whether to accept the data package and certify compliance or request additional work.

The milestone certification data package will contain the following explanations, charts, and data products.:

- (1) A narrative report, including a discussion of how each element of the milestone was met, and a narrative summary of the overall milestone achievement.
- (2) Description of petal design and materials and assembly steps.
- (3) Description of the measurement arm, precision stylus, and calibration certification data (provided by Faro Inc.)
- (4) Description of the metrology process including the process for transferring the base and related intermediate data products, the (x,y) data along the petal edges, and estimates of repeatability.
- (5) Description of the model fitting process and results including error estimates and best fit rms petal shape to the measurements of the petal edge.
- (6) An updated error budget based on the measured petal shape. We will compute the likely contrast achieved assuming the measured petal shape is representative of the global and single-petal errors.
- (7) A calculated image plane pattern assuming global and single-petal errors comparable to those measured on the actual petal.
- (8) If time and resources allow, results of optical edge scatter tests.

APPENDIX A. ON THE ASSUMPTIONS MADE CALCULATING OCCULTER ELECTRIC FIELDS WITH A BESSEL FUNCTION EXPANSION

As discussed in Section 2.1, the electric field at the aperture of a telescope following an occulter can be written as:

$$\begin{aligned}
 E_{\text{occ}}(\rho, \phi) = & E_0 e^{2\pi i z/\lambda} \left(1 - \frac{2\pi}{i\lambda z} \int_0^R A(r) J_0 \left(\frac{2\pi r \rho}{\lambda z} \right) e^{\frac{\pi i}{\lambda z} (r^2 + \rho^2)} r dr \right) \\
 & - E_0 e^{2\pi i z/\lambda} \sum_{j=1}^{\infty} \frac{(-1)^j 2\pi}{i\lambda z} \left(\int_0^R e^{\frac{\pi i}{\lambda z} (r^2 + \rho^2)} J_{jN} \left(\frac{2\pi r \rho}{\lambda z} \right) \frac{\sin(j\pi A(r))}{j\pi} r dr \right) \\
 (9) \quad & \times (2 \cos(jN(\phi - \pi/2)))
 \end{aligned}$$

where λ is the wavelength, N is the number of occulter petals, R is the occulter radius, and (r, θ) and (ρ, ϕ) are polar coordinates at the occulter and telescope planes, respectively. $A(r)$ is the profile defining the occulter shape, which is determined by a linear optimization on a truncated version of $E_{\text{occ}}(\rho, \phi)$ which is equivalent to the electric field from an apodized occulter:

$$(10) \quad E_{\text{apod}}(\rho) = E_0 e^{2\pi i z/\lambda} \left(1 - \frac{2\pi}{i\lambda z} \int_0^R A(r) J_0 \left(\frac{2\pi r \rho}{\lambda z} \right) e^{\frac{\pi i}{\lambda z} (r^2 + \rho^2)} r dr \right).$$

When the optimization is performed, we assume that sufficient petals are present such that $|E_{\text{occ}}(\rho, \phi) - E_{\text{apod}}(\rho)|$ is small, i.e., that our approximation is not neglecting nonlinear terms which will compromise the performance of the occulter when they are included. More generally, the infinite series must always be truncated at some point for any electric field calculation, and we would like to ensure that we are not neglecting important terms.

We approach this problem from two directions. First, we can develop upper bounds which depend only on basic system parameters (N , R , λ , etc.) and are independent of $A(r)$, which show that the series can be truncated after a certain number of terms regardless of the outcome of the optimization. Second, once we have an optimized design, we can calculate the remaining terms explicitly to verify that they are negligible for appropriate choices of N .

In the first case, our criterion is not that the higher-order Bessel terms get small with respect to J_0 but rather that the terms of the series expansion get small with respect to the magnitude of the desired electric field from the occulted starlight $|E_{\text{apod}}(\rho)|$, so that neglecting them doesn't change our estimate of suppression. To do so we will use the following fact of Bessel functions (from Eq. 9.1.62 in [16]):

$$(11) \quad |J_n(x)| \leq \frac{1}{n!} \left(\frac{x}{2}\right)^n$$

with $n \in \mathbb{N}$ and $x \in [0, \infty)$. This allows us to write an absolute upper bound U_j on any of the terms of the expansion using the shortest wavelength:

$$(12) \quad \left| -E_0 e^{2\pi iz/\lambda} \frac{(-1)^j 2\pi}{i\lambda_{\min} z} \left(\int_0^R e^{\frac{\pi i}{\lambda z}(r^2 + \rho^2)} J_{jN} \left(\frac{2\pi r \rho}{\lambda_{\min} z} \right) \frac{\sin(j\pi A(r))}{j\pi} r dr \right) (2 \cos(jN(\phi - \pi/2))) \right|$$

$$(13) \quad \leq \frac{4|E_0|}{j\lambda_{\min} z} \left| \int_0^R e^{\frac{\pi i}{\lambda z}(r^2 + \rho^2)} J_{jN} \left(\frac{2\pi r \rho}{\lambda_{\min} z} \right) \sin(j\pi A(r)) r dr \right|$$

$$(14) \quad \leq \frac{4|E_0|}{j\lambda_{\min} z} \int_0^R \left| r e^{\frac{\pi i}{\lambda z}(r^2 + \rho^2)} \sin(j\pi A(r)) \right| \left| J_{jN} \left(\frac{2\pi r \rho}{\lambda_{\min} z} \right) \right| dr$$

$$(15) \quad \leq \frac{4|E_0|}{j\lambda_{\min} z} \max_{\rho \in [0, \rho_{\max}]} \left| J_{jN} \left(\frac{2\pi R \rho}{\lambda_{\min} z} \right) \right| \int_0^R \left| r e^{\frac{\pi i}{\lambda z}(r^2 + \rho^2)} \sin(j\pi A(r)) \right| dr$$

$$(16) \quad \leq \frac{4|E_0|}{j\lambda_{\min} z} \max_{\rho \in [0, \rho_{\max}]} \left| J_{jN} \left(\frac{2\pi R \rho}{\lambda_{\min} z} \right) \right| \frac{R^2}{2}$$

$$(17) \quad \leq \frac{2|E_0|R^2}{j\lambda_{\min} z} \frac{1}{(jN)!} \left(\frac{\pi R \rho_{\max}}{\lambda_{\min} z} \right)^{jN} \equiv U_j$$

where we also made repeated use of the triangle inequality. These upper bounds are very coarse, and actual values of each term may be significantly smaller. Even so, the $(jN)!$ in the denominator ensures this bound becomes small very rapidly when $\pi R \rho_{\max}/(\lambda_{\min} z) \ll jN$.

In the case of THEIA, for example, $\pi R \rho_{\max}/(\lambda_{\min} z) \approx 14.85$ and $R^2/(\lambda_{\min} z) \approx 29.09$ for $\rho_{\max} = 3.25\text{m}$. Using $N = 20$ (the number of petals in the THEIA occulter) we can evaluate some worst-case upper bounds:

$$(18) \quad U_1 = \frac{2|E_0|R^2}{\lambda_{\min} z} \frac{1}{(N)!} \left(\frac{\pi R \rho_{\max}}{\lambda_{\min} z} \right)^N \approx 6.5 \times 10^6 |E_0|$$

$$(19) \quad U_2 = \frac{2|E_0|R^2}{2\lambda_{\min} z} \frac{1}{(2N)!} \left(\frac{\pi R \rho_{\max}}{\lambda_{\min} z} \right)^{2N} \approx 2.6 |E_0|$$

$$(20) \quad U_3 = \frac{2|E_0|R^2}{3\lambda_{\min} z} \frac{1}{(3N)!} \left(\frac{\pi R \rho_{\max}}{\lambda_{\min} z} \right)^{3N} \approx 4.7 \times 10^{-11} |E_0|$$

$$(21) \quad U_4 = \frac{2|E_0|R^2}{4\lambda_{\min} z} \frac{1}{(4N)!} \left(\frac{\pi R \rho_{\max}}{\lambda_{\min} z} \right)^{4N} \approx 1.1 \times 10^{-24} |E_0|$$

...

As $|E_{\text{apod}}(\rho)|$ within the occulter shadow at the telescope aperture is $\sim 10^{-5}$ for all λ and ρ when $E_0 = 1$, two terms should be sufficient in the absolute worst case to calculate the electric field at

the aperture, regardless of the actual shape of the THEIA occulter. A similar bounding procedure is used in the existing propagation routines to determine when to truncate the series. As a note, the coarse nature of these bounds can be seen by applying the same procedure to $|E_{\text{apod}}(\rho)|$:

$$(22) \quad |E_{\text{apod}}(\rho)| = \left| E_0 e^{2\pi iz/\lambda_{\min}} \left(1 - \frac{2\pi}{i\lambda_{\min}z} \int_0^R A(r) J_0 \left(\frac{2\pi r \rho_{\max}}{\lambda_{\min}z} \right) e^{\frac{\pi i}{\lambda_{\min}z}(r^2 + \rho_{\max}^2)} r dr \right) \right|$$

$$(23) \quad \leq |E_0| + \frac{2|E_0|\pi}{\lambda z} \left| \int_0^R A(r) J_0 \left(\frac{2\pi r \rho}{\lambda_{\min}z} \right) e^{\frac{\pi i}{\lambda_{\min}z}(r^2 + \rho_{\max}^2)} r dr \right|$$

$$(24) \quad \leq |E_0| + \frac{2|E_0|\pi R^2}{\lambda_{\min}z} = \left(1 + \frac{\pi R^2}{\lambda_{\min}z} \right) |E_0| \approx 92.4 |E_0|$$

Once the optimization for an occulter such as THEIA has been completed, we can use the resulting $A(r)$ to calculate exact values of Eq. 12. In the case of the THEIA profile at λ_{\min} and ρ_{\max} :

$$(25) \quad \left| -E_0 e^{2\pi iz/\lambda_{\min}} \frac{(-1)^1 4\pi}{i\lambda_{\min}z} \left(\int_0^R e^{\frac{\pi i}{\lambda_{\min}z}(r^2 + \rho_{\max}^2)} J_{1N} \left(\frac{2\pi r \rho_{\max}}{\lambda_{\min}z} \right) \frac{\sin(1\pi A(r))}{\pi} r dr \right) \right| = 8.6 \times 10^{-4} |E_0|$$

$$(26) \quad \left| -E_0 e^{2\pi iz/\lambda_{\min}} \frac{(-1)^2 4\pi}{i\lambda_{\min}z} \left(\int_0^R e^{\frac{\pi i}{\lambda_{\min}z}(r^2 + \rho_{\max}^2)} J_{2N} \left(\frac{2\pi r \rho_{\max}}{\lambda_{\min}z} \right) \frac{\sin(2\pi A(r))}{2\pi} r dr \right) \right| = 7.7 \times 10^{-9} |E_0|$$

$$(27) \quad \left| -E_0 e^{2\pi iz/\lambda_{\min}} \frac{(-1)^3 4\pi}{i\lambda_{\min}z} \left(\int_0^R e^{\frac{\pi i}{\lambda_{\min}z}(r^2 + \rho_{\max}^2)} J_{3N} \left(\frac{2\pi r \rho_{\max}}{\lambda_{\min}z} \right) \frac{\sin(3\pi A(r))}{3\pi} r dr \right) \right| = 3.6 \times 10^{-18} |E_0|$$

$$(28) \quad \left| -E_0 e^{2\pi iz/\lambda_{\min}} \frac{(-1)^4 4\pi}{i\lambda_{\min}z} \left(\int_0^R e^{\frac{\pi i}{\lambda_{\min}z}(r^2 + \rho_{\max}^2)} J_{4N} \left(\frac{2\pi r \rho_{\max}}{\lambda_{\min}z} \right) \frac{\sin(4\pi A(r))}{4\pi} r dr \right) \right| = 4.9 \times 10^{-31} |E_0|$$

where the angular dependence has been removed—we consider only the $\phi = \pi/2$ case, where the cosine will be maximal for all j . Clearly, the upper bounds in Eqs. 18—21 significantly overestimate the terms of the series; the $j = 2$ can be seen to have a negligible contribution to the field as well. The $j = 1$ term remains significant compared to $|E_{\text{apod}}(\rho)|$, as for λ_{\min} and ρ_{\max} :

$$(29) \quad \left| E_0 e^{2\pi iz/\lambda_{\min}} \left(1 - \frac{2\pi}{i\lambda_{\min}z} \int_0^R A(r) J_0 \left(\frac{2\pi r \rho_{\max}}{\lambda_{\min}z} \right) e^{\frac{\pi i}{\lambda_{\min}z}(r^2 + \rho_{\max}^2)} r dr \right) \right| = 3.7 \times 10^{-4} |E_0|$$

and so there are ϕ -dependent peaks of non-negligible intensity in the image plane. Fortunately, in this case, these peaks turn out not to affect the occulter performance when the full system is simulated; nevertheless, for this reason all optical simulations are done with $|E_{\text{occ}}(\rho, \phi)|$ rather than $|E_{\text{apod}}(\rho)|$.

(As a side note, simulated planets are created by propagating a tilted plane wave past the occulter; this can be shown [15] to be equivalent to shifting the position of the telescope aperture in the on-axis field and adding a tilt across the aperture. The shifted position effectively increases ρ_{\max} , requiring many terms to be retained in the series in order to accurately estimate the field.)

APPENDIX B. FUTURE TECHNOLOGY DEVELOPMENT

As we noted in Section 1, this TDEM was of limited scope and focused on what we consider to be the most important first step—manufacturing and measuring a flight-like petal. There are many other important technology developments required to build confidence in the viability of an occulter-based approach to planet finding. We expect investments to continue in the effort to

advance these critical technologies. This future work should include the following key technology developments:

- Measure and confirm that petals meet the thermal deformation tolerances under the expected temperature changes.
- Refine the requirements and analysis and confirm, through direct measurements on a full size petal, that stray light scatter from the sun is sufficiently low.
- Perform repeated stow and deploy tests of a full-size petal made from flight materials and verify that it maintains the positioning tolerances.
- Manufacture and deploy multiple petals. Follow with a demonstration of the central truss deployment with attached petals. Verify that deployed tolerances are met.
- Develop algorithms for occulter/telescope alignment stationkeeping, included coupled translational and attitude control. Verify through modeling and simulation as well as through hardware-in-the-loop testing using subscale models of the pupil-plane position sensor.
- Analyze and verify that in-plane dynamic deformations meet requirements under varying loads, including before, during, and after thruster firings.

REFERENCES

- [1] D.J. Des Marais, M.O. Harwit, K.W. Jucks, J.F. Kasting, D.N. Lin, J.I. Lunine, J. Schneider, S. Seager, W.A. Traub, and N.J. Woolf. Remote sensing of planetary properties and biosignatures on extrasolar terrestrial planets. *Astrobiology*, 2(2):153–181, 2002.
- [2] Steven V. W. Beckwith. Detecting life-bearing extrasolar planets with space telescopes. *The Astrophysical Journal*, 684(2):1404–1415, 2008.
- [3] L. Spitzer. The beginnings and future of space astronomy. *American Scientist*, 50:473–484, 1962.
- [4] C.J. Copi and G.D. Starkman. The big occulting steerable satellite [BOSS]. *Astrophysical Journal*, 532:581–592, 2000.
- [5] W. Cash. Detection of earth-like planets around nearby stars using a petal-shaped occulter. *Nature*, 442:51–53, 2006.
- [6] R.J. Vanderbei, E.J. Cady, and N.J. Kasdin. Optimal occulter design for finding extrasolar planets. *Astrophysical Journal*, 665:794–798, 2007.
- [7] R.J. Vanderbei, D. Spergel, and N.J. Kasdin. Circularly symmetric apodization via star-shaped masks. *Astrophysical Journal*, 599:686–694, 2003.
- [8] E. Cady, S. Shaklan, N.J. Kasdin, and D. Spergel. A method for modifying occulter shapes. volume 7440. SPIE, 2009.
- [9] N. Jeremy Kasdin, Paul Atcheson, Matt Beasley, Rus Belikov, Morley Blouke, Eric Cady, Daniela Calzetti, Craig Copi, Steve Desch, Phil Dumont, Dennis Ebbets, Rob Egerman, Alex Fullerton, Jay Gallagher, Jim Green, Olivier Guyon, Sally Heap, Rolf Jansen, Ed Jenkins, Jim Kasting, Ritva Keski-Kuha, Marc Kuchner, Roger Lee, Don J. Lindler, Roger Linfield, Doug Lisman, Rick Lyon, John MacKenty, Sangeeta Malhotra, Mark McCaughrean, Gary Mathews, Matt Mountain, Shouleh Nikzad, Bob OConnell, William Oegerle, Sally Oey, Debbie Padgett, Behzad A Parvin, Xavier Prochaska, James Rhoads, Aki Roberge, Babak Saif, Dmitry Savransky, Paul Scowen, Sara Seager, Bernie Seery, Kenneth Sembach, Stuart Shaklan, Mike Shull, Oswald Siegmund, Nathan Smith, Remi Soummer, David Spergel, Phil Stahl, Glenn Starkman, Daniel K Stern, Domenick Tenerelli, Wesley A. Traub, John Trauger, Jason Tumlinson, Ed Turner, Bob Vanderbei, Roger Windhorst, Bruce Woodgate, and Bob Woodruff. THEIA: Telescope for habitable exoplanets and interstellar/intergalactic astronomy. <http://www.astro.princeton.edu/dns/Theia/nas.theia.v14.pdf>.
- [10] D. Savransky, N.J. Kasdin, and D.N. Spergel. Results from the automated design reference mission constructor for exoplanet imagers. volume 7440. SPIE, 2009.
- [11] O. Guyon, J. R. P. Angel, R. Belikov, R. Egerman, D. Gavel, A. Giveon, T. Greene, K. Cahoy, B. Kern, M. Levine, S. Ridgway, S. Shaklan, D. Tenerelli, R. Vanderbei, and R. A. Woodruff. Detecting and characterizing exoplanets with a 1.4-m space telescope: the Pupil mapping Exoplanet Coronagraphic Observer (PECO). In *Society of Photo-Optical Instrumentation Engineers (SPIE) Conference Series*, volume 7440 of *Society of Photo-Optical Instrumentation Engineers (SPIE) Conference Series*, August 2009.
- [12] J. Trauger, K. Stapelfeldt, W. Traub, J. Krist, D. Moody, D. Mawet, E. Serabyn, C. Henry, P. Brugarolas, J. Alexander, R. Gappinger, O. Dawson, V. Mireles, P. Park, L. Pueyo, S. Shaklan, O. Guyon, J. Kasdin, R. Vanderbei, D. Spergel, R. Belikov, G. Marcy, R. A. Brown, J. Schneider, B. Woodgate, R. Egerman, G. Matthews, J. Elias, Y. Conturie, P. Vallone, P. Voyer, R. Polidan, C. Lillie, C. Spittler, D. Lee, R. Hejal, A. Bronowicki, N. Saldivar, M. Ealey, and T. Price. ACCESS: a concept study for the direct imaging and spectroscopy of exoplanetary systems. In *Society of Photo-Optical Instrumentation Engineers (SPIE) Conference Series*, volume 7731 of *Society of Photo-Optical Instrumentation Engineers (SPIE) Conference Series*, July 2010.

- [13] P. Dumont, S. Shaklan, E. Cady, J. Kasdin, and R. Vanderbei. Analysis of external occulters in the presence of defects. volume 7440. SPIE, 2009.
- [14] S. Shaklan, M. C. Noecker, T. Glassman, A. S. Lo, P. J. Dumont, N. J. Kasdin, E. J. Cady, R. Vanderbei, and P. R. Lawson. Error budgeting and tolerancing of starshades for exoplanet detection. In *Proceedings of the SPIE Astronomical Instrumentation Conference*, number 1000 in 7731, 2010.
- [15] E. Cady. Design, tolerancing, and experimental verification of occulters for finding extrasolar planets. PhD Thesis, Princeton University, 2010.
- [16] M. Abramowitz and A. Stegun. *Handbook of Mathematical Functions*. 1972.